



# PdO and PtO loaded WS<sub>2</sub> boosts NO<sub>2</sub> gas sensing characteristics at room temperature

Aanchal Alagh<sup>a</sup>, Fatima Ezahra Annanouch<sup>a,\*</sup>, Khaled Al Youssef<sup>b</sup>, Carla Bittencourt<sup>b</sup>, Frank Güell<sup>c</sup>, Paulina R. Martínez-Alanis<sup>c</sup>, Marc Reguant<sup>c</sup>, Eduard Llobet<sup>a</sup>

<sup>a</sup> Departament d'Enginyeria Electronica, Universitat Rovira i Virgili, avenida Països Catalans 26, 43007 Tarragona, Spain

<sup>b</sup> Laboratory of Plasma-Surface Interaction Chemistry (PSI Chem), University of Mons, Av. Nicolas Copernic 1, 7000 Mons, Belgium

<sup>c</sup> ENFOCAT-IN2UB, Universitat de Barcelona, C/Martí i Franquès 1, 08028 Barcelona, Catalunya, Spain

## ARTICLE INFO

### Keywords:

TMDs  
Functionalization  
Gas sensors  
CVD  
AACVD  
Tungsten disulphide

## ABSTRACT

In this work tungsten disulphide nanostructures loaded with platinum-oxide (PtO), or palladium-oxide (PdO) were grown directly onto alumina substrates. This was achieved using a combination of aerosol-assisted chemical vapour deposition (AA-CVD) method with atmospheric pressure CVD technique. At first, tungsten oxide nano-wires loaded with either PtO or PdO nanoparticles were successfully co-deposited via AA-CVD followed by sulfurization at 900 °C in the next step. The morphological, structural, and chemical characteristics were investigated using FESEM, TEM, XRD, XPS and Raman spectroscopy. The results confirm the presence of PdO and PtO in the WS<sub>2</sub> host matrix. Gas sensing attributes of loaded and pristine WS<sub>2</sub> sensors were investigated, at room temperature, towards different analytes (NO<sub>2</sub>, NH<sub>3</sub>, H<sub>2</sub> etc.). Both pristine and metal-oxide loaded WS<sub>2</sub> gas sensors show remarkable responses at room temperature towards NO<sub>2</sub> detection. Further, the loaded sensors demonstrated stable, reproducible, ultrasensitive, and enhanced gas sensing response, with a detection limit below 25 ppb. Additionally, the effect of ambient humidity on the sensing response of both loaded and pristine sensors was investigated for NO<sub>2</sub> gas. The response of PtO loaded sensor considerably decreased in humid environments, while the response for pristine and PdO loaded sensors increased. However, slightly heating (at 100 °C) the sensors, suppresses the influence of humidity. Finally, the long-term stability of different sensors is investigated, and the results demonstrate high stability with repeatable results after 6 weeks of gas sensing tests. This work exploits an attractive pathway to add functionality in the transition metal dichalcogenide host matrix.

## 1. Introduction

While technological advancements have improved an individual's lifestyle, they have also contributed to the emergence of environmental issues, such as global warming and pollution. In particular, the number of pollutant emissions in the atmosphere has increased dramatically, leading to air pollution [1]. This phenomenon is caused by particulate matter and several harmful gases, including nitrogen dioxide (NO<sub>2</sub>), ammonia (NH<sub>3</sub>), carbon monoxide (CO), sulphur dioxide (SO<sub>2</sub>), hydrogen sulphide (H<sub>2</sub>S), carbon monoxide (CO), and ozone (O<sub>3</sub>) [2]. These gases not only pose a threat to the environment but are also detrimental to human health, as they are a leading cause of ailments such as respiratory irritation syndrome, lung diseases, and bronchitis, only to name a few. According to research, air pollution is responsible for one out of every nine deaths each year, making it the leading cause of

death. Besides, around 92% of the world's population lives in areas with poor air quality, putting them at significant risk of premature death [3]. Furthermore, among all, NO<sub>2</sub> is one of the life-threatening contaminants. Therefore, the legitimate airborne permissible exposure limit of NO<sub>2</sub>, as stipulated by the Occupational Safety and Health Administration (OSHA) is 5 ppm, which cannot be surpassed [4]. Also, the American Industrial Hygiene Association has set a 5-minute emergency exposure limit for NO<sub>2</sub> at 35 parts per million (ppm) as exposure above this concentration can cause skin damage and respiratory issues [5]. Therefore, it is now more important than ever to regularly monitor and evaluate the air quality.

In this respect, gas sensing devices play an essential role in the detection and monitoring of poisonous pollutants like NO<sub>2</sub> to reduce their damaging effects. Based on their working mechanism, these devices are categorised into chemoresistive, optical, electrochemical, and

\* Corresponding author.

E-mail address: [fatimaezahra.annanouch@urv.cat](mailto:fatimaezahra.annanouch@urv.cat) (F.E. Annanouch).

<https://doi.org/10.1016/j.snb.2022.131905>

Received 31 January 2022; Received in revised form 2 April 2022; Accepted 13 April 2022

Available online 16 April 2022

0925-4005/© 2022 The Author(s). Published by Elsevier B.V. This is an open access article under the CC BY-NC-ND license (<http://creativecommons.org/licenses/by-nc-nd/4.0/>).

gravimetric (e.g., micro-cantilever) sensors. Among them, the chemoresistive type gas sensors have obtained broad consideration as they offer significant advantages over other sensors in terms of their simple fabrication, ease of operation and affordable cost. In general, these sensors are based on metal oxide semiconductors (MOX), thanks to their excellent gas-sensing performance towards harmful gases, such as  $\text{NH}_3$ ,  $\text{H}_2\text{S}$  and  $\text{CO}$  [6]. However, conventional MOX chemoresistive sensors typically work at elevated temperatures above  $200^\circ\text{C}$ , which along with high power consumption brings a huge hindrance to their portability and long-run reliability [7]. As a result, in the last few years, considerable efforts have been directed towards the development of room temperature gas sensors for application in consumer electronics, wearables and wireless sensing networks.

Consequently, 2D materials like inorganic analogues of graphene (GR), such as transition-metal dichalcogenides (TMDs), have emerged as a viable material for gas sensing applications. Similar to GR, this class of materials have a layered structure. They have X-M-X architecture, where M is a transition metal atom and X is a chalcogen atom, however, unlike GR, they do not have a single layer of atoms. The chalcogen atoms are arranged in two hexagonal planes separated by a plane of metal atoms, forming sandwich structures. The atoms in these three layers are bonded together by strong covalent connections, whereas each three-layer sheet is attached to its neighbouring atoms by weak Van der Waals forces of attraction. Moreover, TMDs, unlike other carbon-based 2D structures (such as GR), have an inherent energy bandgap, which gives them remarkable chemical and electrical characteristics [8]. As a result, these materials are extremely useful in a variety of sectors including aerospace, military, semiconductor, automotive, and medicine. For instance, they are utilized as a photovoltaic material for solar cell application [9], light-emitting devices [10], transistors [11], diodes and many more.

While there has been a recent spike in interest in the synthesis and study of TMDs thin films, most of these studies have focused on  $\text{MoS}_2$  and  $\text{WS}_2$ . 2D layered tungsten disulphide, on the other hand, has fascinated the gas sensing community with its remarkable electrical and optoelectronic capabilities. A two-dimensional layer of  $\text{WS}_2$  is made up of covalently bound W-S atoms that are stacked together by a weak Van der Waals interaction [13], which permits gases to diffuse smoothly in between the layers. Furthermore, because of its large surface area and active gas adsorption sites (edges, vacancies, and surface defects), its 2D structure outperforms conventional MOX-based gas sensors at significantly lower operating temperatures [3,6,12]. It is not only due to its unique features, but also to the ease with which these properties may be tuned through dimension control, surface design, and doping.

However, despite all the above-stated properties, pristine  $\text{WS}_2$  shows poor gas sensing response at room temperature, this is due to the strong adsorption of gas molecules on the  $\text{WS}_2$  surface which leads to partial desorption of these molecules during the recovery cycle, resulting in much longer response time with low sensing response. Hence, limiting the practical applications of pristine  $\text{WS}_2$  based gas sensors in the real environment [12,13].

In MOX chemoresistors, loading the active layer with noble metals is a successful way to enhance the gas sensing performance, as these noble metals can induce electronic and chemical sensitization effects at the surface of the host matrix. Catalytic metal particles increase the number of active sites and lower the activation energy for gas adsorption, resulting in higher adsorption rates and lower operating temperatures. Subsequently, improved sensing response, better recovery characteristics and enhanced selectivity are achieved [14–16]. A similar approach has also been reported for enhancing the sensing response of TMDs. The dispersion of noble metal particles on the surface of TMDs creates spill-over effects that aid to increase the rate of surface reactions, resulting in faster response and recovery times [17]. For instance, it has been reported that loading  $\text{WS}_2$  nanosheets with Ag nanowires dramatically improves the sensing response with a 12-fold increase (667%) towards  $\text{NO}_2$  exposure via a spillover effect [18]. Similarly, a study of Au decorated  $\text{WS}_2$  nanosheets reported enhanced sensing

response towards CO using very low power consumption ( $28.6\ \mu\text{W}$ ), which is attributed to the spillover effect brought about by Au NPs. Moreover, the sensor showed enhanced selectivity towards CO owing to the catalytic effect of Au NPs [13]. Decoration of  $\text{WS}_2$  with  $\text{WO}_3$  NPs via layer-by-layer self-assembly technique displayed enhanced gas sensing results. The response values of  $\text{WS}_2$ ,  $\text{WO}_3$ , and  $\text{WS}_2/\text{WO}_3$ -LbL sensors toward 10 ppm of ethanol gas were 37.82%, 14.88%, and 74.50%, respectively. The enhanced sensing performance towards ethanol detection is attributed to the  $\text{WS}_2/\text{WO}_3$  heterojunction unique charge-transfer properties as well as the synergistic effects of the two materials [19]. Moreover, our recent study on  $\text{Cu}_2\text{O}$  doped  $\text{WS}_2$  also revealed enhanced gas sensing properties (11-fold increase in the sensor response) towards  $\text{H}_2\text{S}$  gas detection. Herein, the proposed gas sensing mechanism is based on the p-p heterojunction formed between the two materials. [20]. Even though the literature reviewed above indicates that the modification of TMDs results in enhanced gas sensing properties, there is a need for sensors that work at room temperature and are simple to fabricate.

To date, a variety of methods have been explored to graft functional groups or complex molecules onto pristine TMDs, such as plasma treatment [22], [23], low-energy ion implantation/substitutional doping [24], [25], and covalent or non-covalent functionalization [26]. However, each method has its limitations. For instance, substitutional doping causes defects in the TMD structure [27], [28]. Another study suggests functionalisation of TMDs flakes with different solutions to achieve the effect of doping, nevertheless, the procedure is often difficult and time-consuming [29], [30]. Moreover, doping with plasma has also been reported in previous studies, resulting in defect formation along with a considerable reduction in charge mobility [22], [23]. Sputtering is another technique that is widely used for depositing metal/metal oxide NPs. Besides, the use of sputtering equipment is involved, and the overall operating cost is high. As a result, it is necessary to investigate efficient loading strategies that are stable, simple to perform, and do not result in severe defects appearing in the TMD material.

Alternatively, inspired by our previous research works [31,32], deposition via aerosol-assisted chemical vapour deposition (AACVD) is an excellent choice to incorporate metal additives on the TMD host matrix. Indeed, it allows us to simultaneously incorporate two or more materials along the host matrix, using one step deposition. It is easy and practical compared to the above-mentioned techniques. Moreover, by combining CVD with AACVD, we can directly grow the sensing material onto the sensor transducer, resulting in a high growth yield, uniform coverage and stable gas sensing responses. Besides, the direct growth of these films, which has a high degree of scalability and controllability, makes nanostructure production considerably closer to mass production.

In this regard, we propose for the first time, the successful growth of tungsten disulphide nanosheets loaded with PdO and PtO materials, using the combination of AACVD and CVD methods for the fabrication of room temperature  $\text{NO}_2$  gas sensor. Throughout the paper, loaded sensors are either denoted by  $\text{WS}_2/\text{PtO}$  (platinum-oxide) or  $\text{WS}_2/\text{PdO}$  (palladium-oxide) whereas pristine sensors are denoted by  $\text{WS}_2$ . Tungsten oxide nanowires loaded with PtO and/or PdO nanoparticles were co-deposited via aerosol-assisted chemical vapour deposition, followed by sulfurization at  $900^\circ\text{C}$  in the corresponding step. The sensing films were then characterised by FESEM, TEM, XRD, Raman spectroscopy, PL spectroscopy and X-ray photoelectron spectroscopy (XPS) to verify the material characteristics of pristine and loaded nanostructures. Moreover, the gas sensing properties of pristine and loaded  $\text{WS}_2$  sensors were investigated and compared towards  $\text{NO}_2$  detection under both dry and humid atmospheres. Additionally, the selectivity of the fabricated sensors was also studied by exposing them to different analytes such as  $\text{NH}_3$ ,  $\text{H}_2\text{S}$ ,  $\text{CO}$  and  $\text{H}_2$ . To the best of our knowledge, no previous reports have described the synthesis of platinum (PtO), or palladium (PdO) loaded  $\text{WS}_2$  adopting the methodology we exploited in our study. Finally, the underlying gas sensing mechanism for the loaded  $\text{WS}_2$  nanostructures is

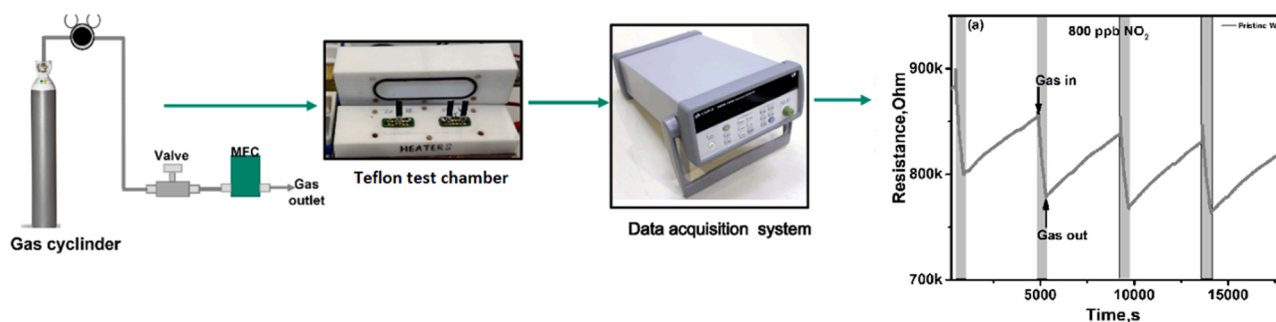


Fig. 1. Gas sensing measurement system setup.

also discussed in detail.

## 2. Experimental section

### 2.1. Material synthesis

Multi-layered nanosheets of pristine and/or loaded  $\text{WS}_2$  films were grown in two steps.

#### 2.1.1. First step deposition using aerosol-assisted chemical vapour deposition technique (AACVD)

In the first step, either pristine or metal-oxide NPs loaded nanowires of  $\text{WO}_3$  were grown, directly on a commercial alumina substrate, with screen-printed, interdigitated platinum electrodes on one side and a platinum resistor heater on the backside. It is a one-step growth process achieved via AACVD method. This technique is widely used to deposit nano and microstructures of metal oxides (Fig. S1 gives a pictorial description of the complete process). Pristine nanowires of  $\text{WO}_3$  were grown using 50 mg of tungsten hexacarbonyl ( $\text{WCO}_6$ ) dissolved in a solution of 15 mL acetone (CAS: 67–64–1) and 5 mL methanol (CAS: 67–56–1). The solution was kept in an ultrasonic bath for 20 min. After the solution was fully solubilised, it was placed in an ultrasonic bath to convert the solution to an aerosol. Nitrogen ( $\text{N}_2$ ) was used as a carrier gas and the flow rate was set to 0.5 L/min to transport the aerosol to the deposition chamber, where the alumina substrate was kept. Before this, the deposition chamber was heated to a temperature of 400 °C. The growth process took approximately 30 min to complete. Afterwards, the chamber was allowed to naturally cool down and later the substrate with  $\text{WO}_3$  nanowires was annealed at 500 °C for 2 h using a carbolite CWF 1200 muffle furnace. Annealing was done to remove any carbon residual left from the precursor, resulting in fully oxidised  $\text{WO}_3$  nanowires.

Metal-oxide NPs loaded nanowires were fabricated adopting the same procedure and equipment as described for the deposition of pristine  $\text{WO}_3$  nanowires. However, the solution containing precursors and the amount of organic solvent used varied. For instance, in the case of  $\text{PdO}/\text{WO}_3$ , 25 mg of  $\text{W}(\text{CO})_6$  was dissolved in 9 mL acetone and 5 mg of palladium acetylacetonate ( $\text{Pd}(\text{C}_5\text{H}_7\text{O}_2)_2$ ) was dissolved in 3 mL methanol separately. The solutions were then mixed and sonicated for 15–20 mins, whereas for  $\text{PtO}/\text{WO}_3$ , 25 mg of  $\text{W}(\text{CO})_6$  was dissolved in 9 mL acetone and 36 mg platinum acetylacetonate ( $\text{Pt}(\text{O}_2\text{C}_5\text{H}_7)_2$ ) was dissolved in 3 mL methanol separately. Again, the two solutions were then mixed and sonicated for 15–20 mins. After this, the same procedure was followed as described previously for growing pristine  $\text{WO}_3$  nanowires. However, for growing metal-oxide loaded nanowires the deposition chamber was heated to a temperature of 350 °C only instead of 400 °C.

#### 2.1.2. Second step deposition using atmospheric pressure chemical vapour deposition technique (CVD)

In the second step of the synthesis, the as-grown  $\text{WO}_3$  nanowires are sulfurized to form  $\text{WS}_2$  nanomaterial using a quartz tube furnace via atmospheric pressure chemical vapour deposition technique (CVD). This

experiment is performed inside an in-house custom built CVD reactor under hydrogen-free conditions (Fig. S2). Preceding the sulfurization process, the quartz tube is flushed with 0.5 L/min of argon gas to remove any oxygen content present in the reactor. Two ceramic boats containing an equal amount of sulphur (S) powder each (>99.95%, Sigma Aldrich, CAS: 7704–34–9) are placed at different temperature zones of the deposition furnace. One of which is placed inside a secondary semi-sealed quartz tube next to the  $\text{WO}_3$  nanowires and the other sulphur boat is placed outside the secondary quartz tube. The boat outside the secondary quartz tube is placed upstream of the argon flow inside the bigger quartz tube. This promotes the double sulfurization of the as-grown  $\text{WO}_3$  nanowires. The furnace is then heated from room temperature to 900 °C with a heating rate of 40 °C/min to remove contaminants such as water or residual organics. This is done to obtain the nucleation of  $\text{WS}_2$ . The growth of  $\text{WS}_2$  is achieved by allowing the reaction to proceed at 900 °C for 60 min under a constant flow of argon. It is vital to control all the growth parameters including the gas flow rate, heating rate and the quantity of sulphur powder used to obtain homogeneously sulfurized multi-layered films of  $\text{WS}_2$ . After the growth phase, the furnace is cooled naturally to room temperature.

Metal-oxide loaded nanowires were sulfurized adopting the same procedure and equipment as described for the sulfurization of pristine  $\text{WO}_3$  nanowires.

### 2.2. Material characterization techniques

The morphology of the as-grown  $\text{WO}_3$  nanowires loaded with PtO or PdO NPs were examined using a transmission electron microscope (JEOL 1011) and a field-emission scanning electron microscope (FESEM) Hitachi 2000 and FEI Helios Nanolab 650. Furthermore, once the films were sulfurized, they were again examined using FESEM. For crystalline phase analysis, XRD measurements were made, using a Bruker-AXS D8-Discover diffractometer equipped with a parallel incident beam (Göber mirror), vertical XYZ motorized stage and with a GADDS (General Area Diffraction System). The elemental and chemical composition was studied via X-ray photoelectron spectroscopy (XPS) using a versaprobe PHI5000 spectrometer (equipped with a monochromatic Al K $\alpha$  X-ray source). For spectrum analysis, the CASA XPS software was used. The Raman spectroscopy measurements were obtained using a Renishaw in Via, laser 514 nm, ion argon-Novatech, 25 mW. Moreover, Photoluminescence measurements at room temperature were also made using a chopped Kimmon IK Series He-Cd laser (325 nm and 40 mW). Fluorescence was dispersed with an Oriel Corner Stone 1/8 74000 monochromator, detected using a Hamamatsu H8259–02 with a socket assembly E717–500 photomultiplier, and amplified through a Stanford Research Systems SR830 DSP. A filter in 360 nm was used to stray light. All spectra were corrected for the response function of the setups.



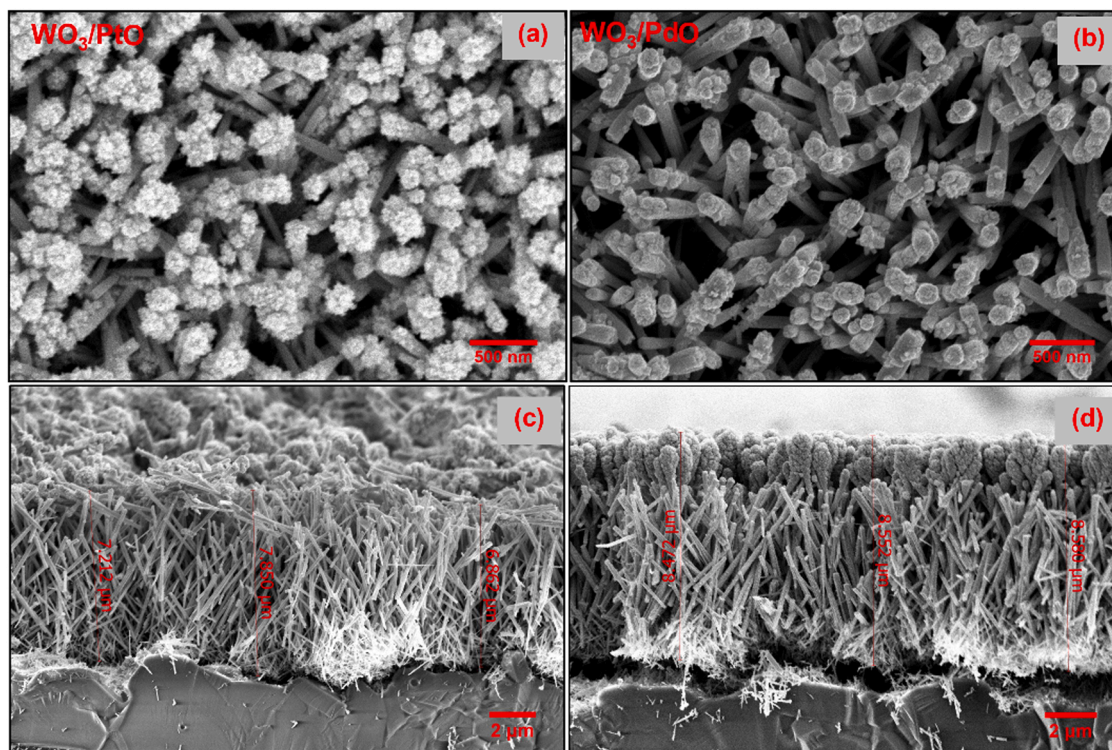


**Fig. 2.** FESEM images of  $\text{WO}_3$  nanoneedles decorated with (a) PtO, (b) PdO nanoparticles. Cross-section image depicting vertically aligned (c) pristine (d) metal-oxide NPs loaded on  $\text{WO}_3$ .

### 2.3. Gas sensing tests

The gas sensing characteristics of the as-fabricated loaded and pristine  $\text{WS}_2$  sensors were measured using a homemade detection system. Commercial alumina substrates with interdigitated platinum electrodes (with 300  $\mu\text{m}$  electrode gap) on the front side and a platinum resistive heater meander on the backside were used to grow either PtO or PdO loaded  $\text{WO}_3$  nanowires which were later sulfurized to grow pristine or loaded films of  $\text{WS}_2$ . The as-fabricated sensors were then tested under a continuous gas flow (100 sccm) in a Teflon test chamber (35 mL in volume) that can accommodate four sensors simultaneously. This testing chamber was connected to a fully automated, continuous gas flow measurement set-up, able to supply diluted gas mixtures as well as humidified gas mixtures using mass flow controllers. An illustration of a typical gas measurement setup is shown in Fig. 1. The gases employed for testing were used from calibrated gas cylinders balanced in dry synthetic air. Unless otherwise specified, all the gas sensing measurements were performed at room temperature.

The sensing measurements consisted of monitoring the change in electrical resistance of the sensor upon exposure to different concentrations of various analytes (such as  $\text{NO}_2$ ,  $\text{NH}_3$ ,  $\text{H}_2$ ,  $\text{CO}$ ,  $\text{H}_2\text{S}$ ) performing up to four replicates for each analyte concentration. The electrical resistance was measured by using an Agilent-34972A multimeter. The sensors were exposed to a given analyte for 10 min and subsequently, the chamber was purged with dry air for 110 min to recover initial baseline resistance. The time left to recover the initial baseline resistance was kept longer purposely since gas sensing measurements were done at room temperature, and desorption of gas molecules takes generally longer than when sensors are operated at elevated temperatures. Sensors were kept overnight in a dry air flow to better stabilise their baseline resistance every time they had to be exposed to a new target gas. The total flow rate was kept constant at a value of 100 mL/min throughout the measurements. Some experiments were also conducted under a humid background (e.g., 50% RH at room temperature, i.e., 21°C) to investigate the humidity interference. This humidity level

was kept constant while exposing the sensor to different concentrations of  $\text{NO}_2$  gas.

## 3. Results and discussion

### 3.1. Structural and morphological characteristics

AACVD of pure  $\text{W}(\text{CO})_6$  and/or a mixture of  $\text{W}(\text{CO})_6$  with Pd ( $\text{C}_5\text{H}_7\text{O}_2$ )<sub>2</sub> and/or Pt ( $\text{O}_2\text{C}_5\text{H}_7$ )<sub>2</sub> resulted in the formation of adherent uniform films of tungsten trioxide nanoneedles and/or tungsten trioxide nanoneedles loaded with PdO and/or PtO nanoparticles, grown directly onto commercial alumina sensor substrates. The as-grown films were initially dark blue while after annealing, they change to pale green for tungsten oxide, brown for tungsten trioxide decorated with palladium-oxide nanoparticles, and off-white for the tungsten trioxide decorated with platinum-oxide nanoparticles. Once these films have been sulfurized the colour for all the samples changes to dark black confirming the formation of  $\text{WS}_2$ .

A field-emission scanning electron microscope (FESEM) was used to characterise the as-deposited films before and after sulfurization. Fig. 2a and b show the FESEM imaging results of the as-synthesised material loaded with either PtO or PdO NPs. It was observed that loading the material with different nanoparticles did not affect the morphology resulting in 60–120 nm thick nanoneedles with similar structures. Moreover, a cross-section of the loaded and pristine films was obtained using an ETD detector installed in the FESEM. The results (Fig. 2c-d) show a small difference in morphology and film thickness between loaded and pristine materials. As depicted in Fig. 2c, pristine nanomaterial consists of 60–120 nm thick nanoneedles with a film thickness of roughly 6–7  $\mu\text{m}$ . After decorating, the nanoneedles are loaded with nanoparticles along with their bodies, as well as an accumulation of these nanoparticles at their tips, resulting in an 8–9  $\mu\text{m}$  film thickness, as seen in Fig. 2d. Furthermore, the nanoneedles were found to be vertically aligned, slanted, and dispersed equally across the entire substrate.

The as-grown films containing  $\text{WO}_3$  nanoneedles were also analysed



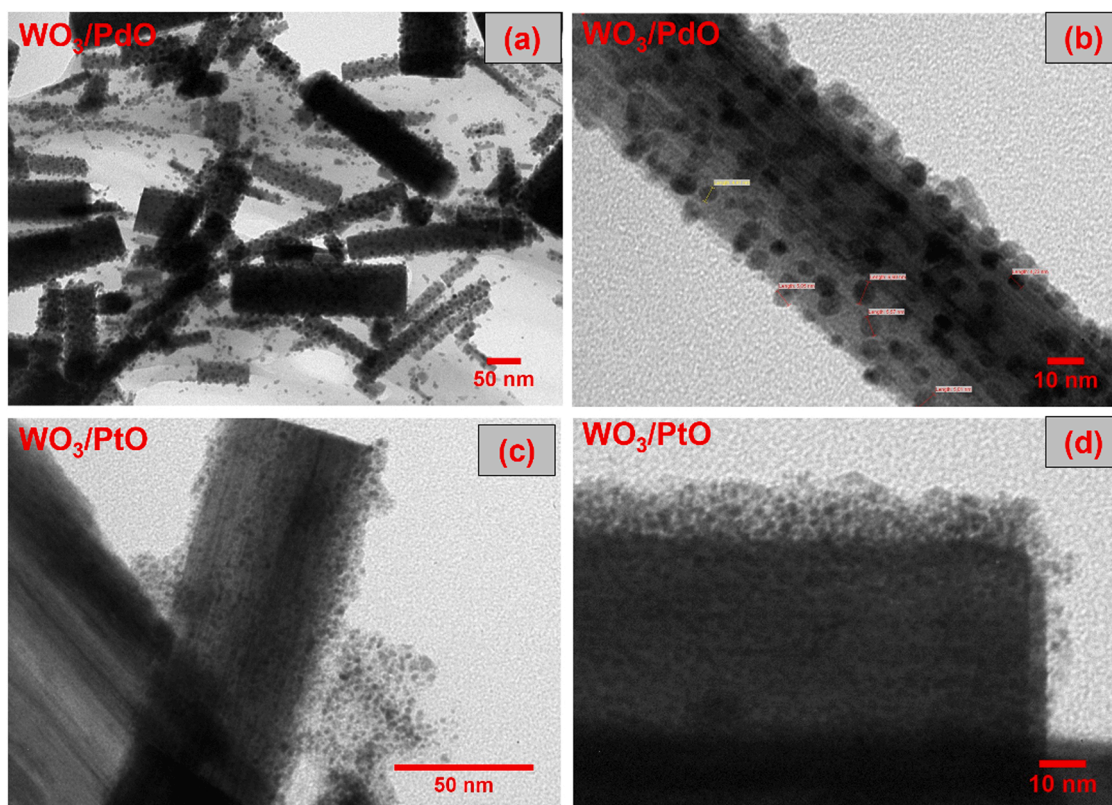


**Fig. 3.** TEM imaging results depicting  $\text{WO}_3$  nanoneedles (NNs) decorated with nanoparticles of (a and b) palladium oxide, having a particle size in the range of 4–6 nm and (c and d) platinum oxide with significantly smaller size in the range of 1–2 nm.

using TEM before sulfurization. The films were scraped from the alumina substrate and deposited over carbon-coated copper grids for analysis. As shown in Fig. 3, the nanoneedles were randomly aligned and uniformly decorated with PdO and/or PtO NPs, indicating that the tungsten oxide nanoneedles had been loaded with well-dispersed metal-oxide NPs. The diameter of the NPs was between 4 and 6 nm in the case of PdO decorated nanoneedles, as shown in Fig. 3a and b, but significantly smaller (1–2 nm) in the case of PtO NP decoration, as shown in Fig. 3c and d.

Following that, the annealed films were sulfurized in a CVD chamber using the methodology described earlier. The films were then examined using FESEM, revealing a change in surface morphology from nanoneedles to nano triangles (in pristine  $\text{WS}_2$ ), nanoflakes (in  $\text{WS}_2/\text{PtO}$ ), and nanoplatelets (in  $\text{WS}_2/\text{PdO}$ ). The NPs were not visible at the surface after sulfurization, as they had been before. The arrangement of nanomaterial that forms nanotriangles in pristine  $\text{WS}_2$  is depicted in Fig. 4a and b, whereas the morphology obtained in loaded films differ slightly, as shown in Fig. 4b–f.

The sensor substrate is uniformly covered with nanoflakes that seem considerably thinner with defined shape and sharp edges with PtO loading, whereas the shape of these nanosheets changes to hexagonal nanoplatelets that are randomly oriented covering the entire substrate with PdO loaded  $\text{WS}_2$ . As a result, the differences in the two morphologies could be linked to differences in the initial morphology of  $\text{WO}_3$  nanocomposite (nanoparticles size) as well as the film composition (different functionalization sources). A cross-section of the sulfurized films was also obtained, revealing film thickness in the 30–32  $\mu\text{m}$  range, as shown in Fig. 4g.

The structural and chemical characteristics of the loaded and pristine films were also evaluated using Raman spectroscopy. In all three samples, Raman features confirm the formation of  $\text{WS}_2$ . Fig. 5a corresponds to the Raman spectra obtained for pristine and loaded  $\text{WS}_2$ , using a 514 nm excitation wavelength laser.  $\text{E}_2^1\text{g}$  and  $\text{A}_1\text{g}$  are the two typical

Raman modes, with the former representing in-plane vibrations of S and W atoms and the latter representing out-of-plane vibrations of S atoms. These two typical Raman modes of pristine  $\text{WS}_2$ ,  $\text{E}_2^1\text{g}$  and  $\text{A}_1\text{g}$  appear at 349 and 415  $\text{cm}^{-1}$  respectively [13,32]. The loaded samples, on the other hand, show a small upshift in both modes, with the  $\text{E}_2^1\text{g}$  of  $\text{WS}_2/\text{PtO}$  and  $\text{WS}_2/\text{PdO}$  samples shifting by 1  $\text{cm}^{-1}$  (from 349 to 350  $\text{cm}^{-1}$ ) and 6  $\text{cm}^{-1}$  (from 349 to 355  $\text{cm}^{-1}$ ) respectively, which can be attributed to the effect of adding functionality [3]. Likewise, an upshift of  $\text{A}_1\text{g}$  band by 1  $\text{cm}^{-1}$  (i.e., from 415 to 416  $\text{cm}^{-1}$ ) and 4  $\text{cm}^{-1}$  (i.e., from 415 to 419  $\text{cm}^{-1}$ ) was also observed for PtO and PdO loaded  $\text{WS}_2$  films, respectively. In contrast, two broad peaks with very low intensity were observed at 693  $\text{cm}^{-1}$  and 806  $\text{cm}^{-1}$  for pristine  $\text{WS}_2$  film, and at 696  $\text{cm}^{-1}$  and 800  $\text{cm}^{-1}$  for  $\text{WS}_2/\text{PtO}$  film. These peaks are indicative of the presence of some  $\text{WO}_3$  impurities, as previously reported [11,13]. Whereas, in the  $\text{WS}_2/\text{PdO}$  material, no such peaks were discovered. However, additional characterisation results discussed below also confirm the presence of tungsten oxide in  $\text{WS}_2/\text{PdO}$ . In our previous results [33], we have observed such impurities ( $\text{WO}_3$ ) in the  $\text{WS}_2$  samples. They can be originated from the uncompleted sulfurization process as well as the presence of some oxygen traces inside the CVD tube since the growth occurs at atmospheric pressure.

For both pristine and loaded  $\text{WS}_2$  films, the ratio of  $\text{A}_1\text{g}$  to  $\text{E}_2^1\text{g}$  peaks remains constant at 0.84, suggesting the formation of multi-layered  $\text{WS}_2$ . The crystallinity of the multi-layered film is further shown by the strong Raman peaks. Also, the Raman analysis results are consistent with those found in prior studies [17,19].

Furthermore, X-ray powder diffraction was used to detect the crystallographic phase of the films. The XRD diffractograms of a pristine  $\text{WS}_2$  sample (upper panel) was compared to those of  $\text{WS}_2/\text{PtO}$  (middle panel) and  $\text{WS}_2/\text{PdO}$  (lower panel) nanostructured films in view of checking for the presence of additional peaks in loaded samples and the results are depicted in Fig. 5b. The three diffractograms obtained were perfectly indexed to the 3R- $\text{WS}_2$  (JCPDOS card no. 01-084-1399). In the  $\text{WS}_2/$

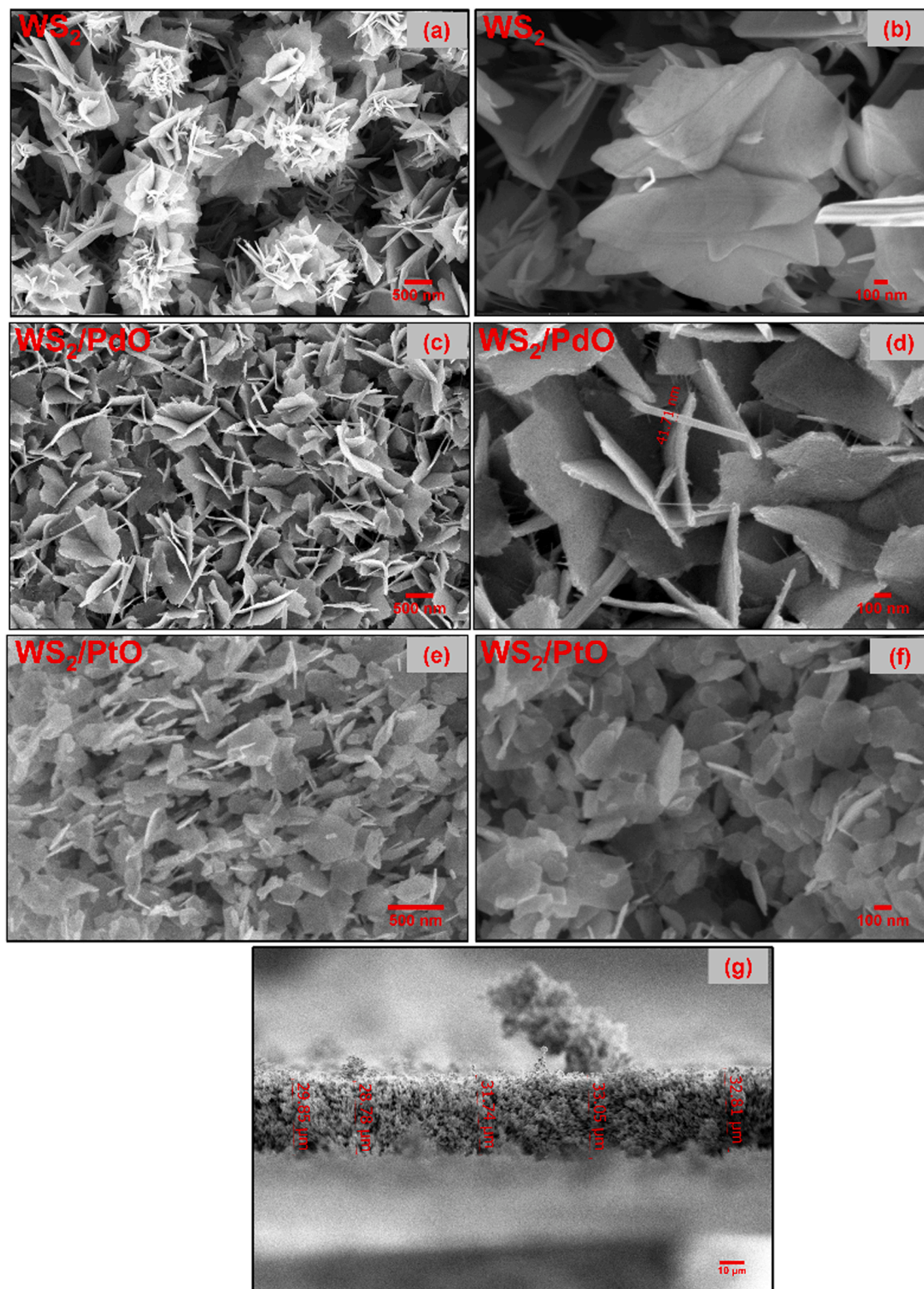


Fig. 4. FESEM images (a and b) pristine  $\text{WS}_2$  (c and d)  $\text{WS}_2/\text{PdO}$ , (e and f)  $\text{WS}_2/\text{PtO}$  NPs. Cross-section image depicting  $\text{WS}_2$  film thickness (g).

$\text{PdO}$  sample, some additional low-intensity diffraction peaks suggesting the presence of  $\text{PdO}$  were also discovered. These peaks indicate the presence of tetragonal  $\text{PdO}$  (002) at  $2\theta$  of 33.54 (JCPDOS card no. 41–1107). Additionally, a small peak at  $2\theta$  of 23.1(002) was also found in this sample, indicating the presence of  $\text{WO}_3$  impurities. For the  $\text{WS}_2/\text{PtO}$  sample, peaks at  $2\theta$  of 33.5 (002) and 41.4 (110) indicate the presence of tetragonal  $\text{PtO}$  (JCPDOS card no. 43–1100). Whereas some

additional peaks with low intensity indicating the presence of  $\text{PtS}$  in low quantity were also observed at  $2\theta$  of 29.59 (101) and 47.52 (112) (JCPDOS card no. 26–1302) in  $\text{PtO}$  decorated  $\text{WS}_2$ . Furthermore, some peaks corresponding to the alumina substrate were present in all three samples, however, peaks from any other impurity were not detected, indicating that a well crystallised single-phase  $\text{WS}_2$  was obtained.

The room-temperature photoluminescence (PL) spectra for  $\text{WO}_3$



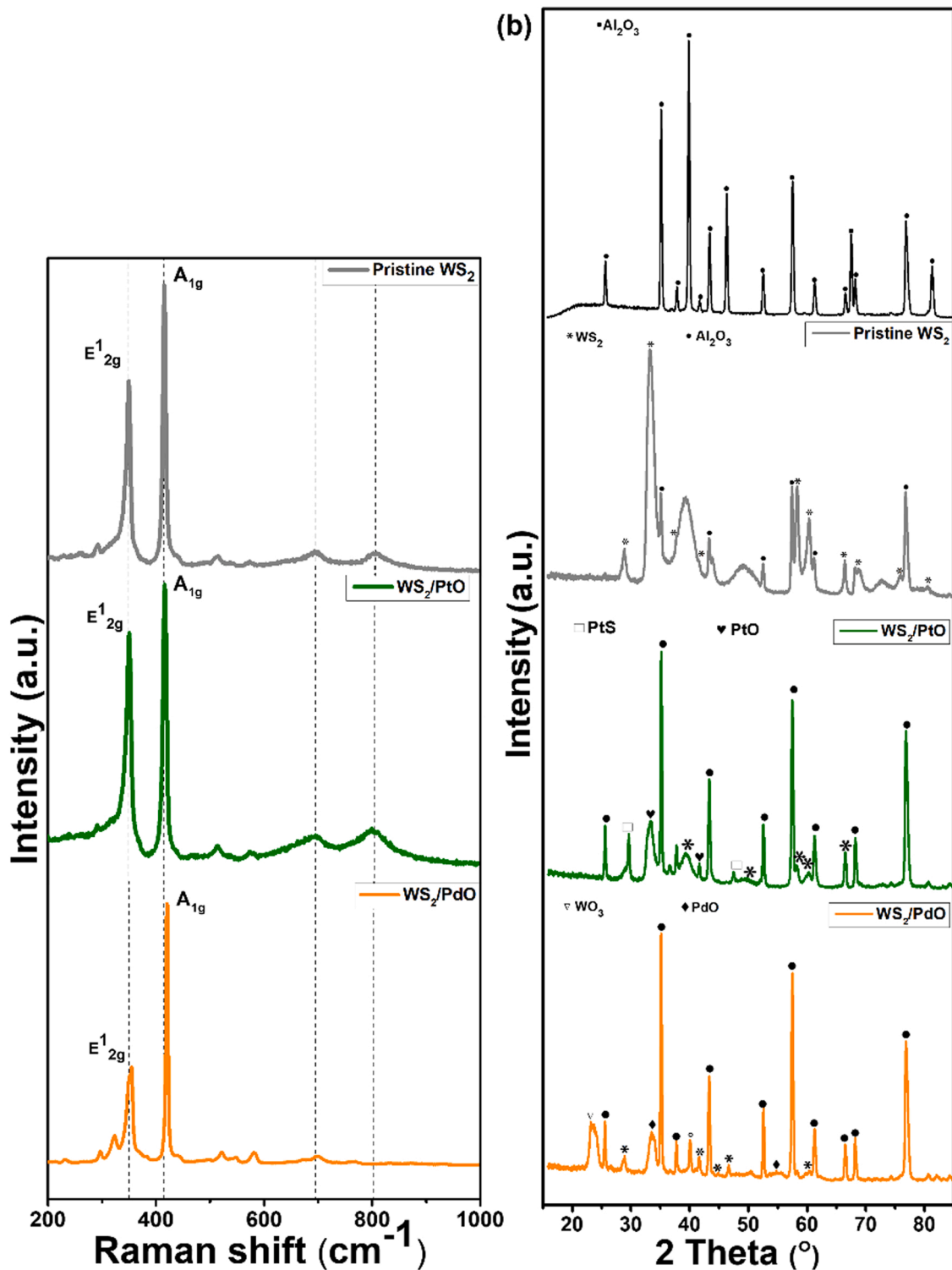


Fig. 5. (a) Raman spectra and (b) XRD diffractograms of pristine WS<sub>2</sub>, WS<sub>2</sub>/PtO and WS<sub>2</sub>/PdO NPs.

decorated either with PtO or PdO NPs and WS<sub>2</sub> loaded either with PtO or PdO are presented in Fig. 6a and b respectively. The intensity of each spectrum was normalized to the maximum emission intensity for relative comparison. By pumping at 325 nm, we observed an emission peak of WO<sub>3</sub> nanoneedles at around 450 nm (2.75 eV) with a full width at half maximum (FWHM) of 370 meV (Fig. 7a). When loading the WO<sub>3</sub> nanoneedles with the PdO or PtO NPs, the emission peak is shifted to 490 nm (2.53 eV) and 530 nm (2.34 eV) and the FWHM are around 540 and 660 meV, respectively. This broadening observed on the FWHM

indicates that the quantity of intrinsic defects is higher when loading the WO<sub>3</sub> NWs with the PdO or PtO NPs. On the other hand, by pumping at 325 nm, we observed an emission peak of WS<sub>2</sub> nanostructures at around 393 nm (3.16 eV) with a full width at half maximum (FWHM) of 440 meV (Fig. 6b). When loading the WS<sub>2</sub> nanostructures with the PdO or PtO NPs, the emission peak is shifted to 430 nm (2.88 eV) and 461 nm (2.69 eV) and the FWHM are around 540 and 480 meV, respectively. This broadening observed on the FWHM indicates that the quantity of intrinsic defects is higher when loading the WS<sub>2</sub> nanostructures with the



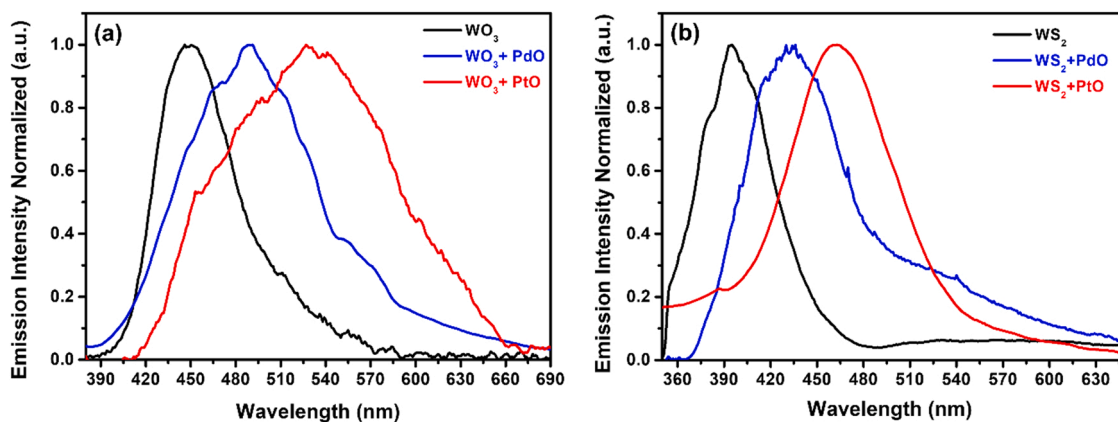


Fig. 6. PL spectra of (a) pure  $\text{WO}_3$ ,  $\text{WO}_3/\text{PdO}$  and  $\text{WO}_3/\text{PtO}$ , (b) pristine  $\text{WS}_2$ ,  $\text{WS}_2/\text{PdO}$  and  $\text{WS}_2/\text{PtO}$ .

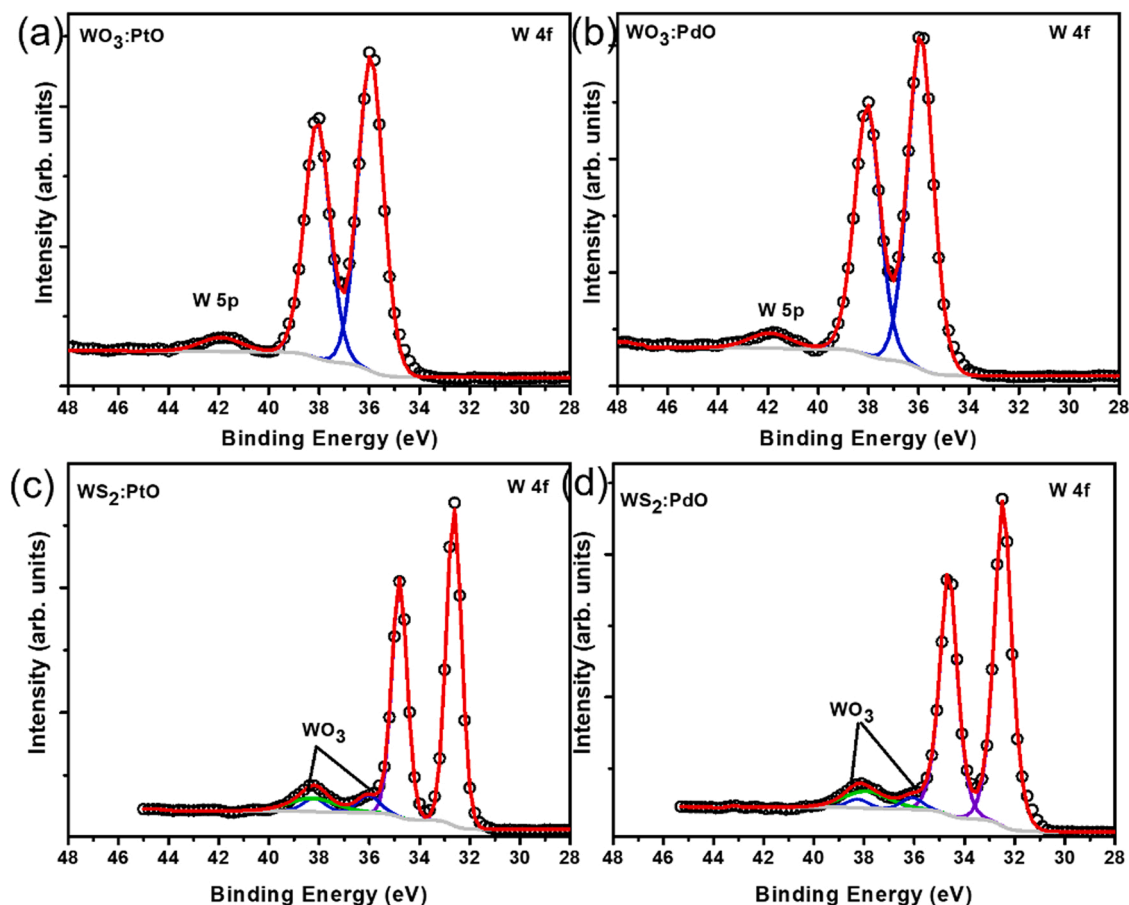


Fig. 7. XPS W 4f core level (a)  $\text{WO}_3$ : PtO (b)  $\text{WO}_3$ : PdO (c)  $\text{WS}_2$ : PtO (d)  $\text{WS}_2$ : PdO.

PdO or PtO NPs. Emission peaks at around 393 nm (3.16 eV), 420 nm (2.95 eV) and 461 nm (2.69 eV) were previously observed in  $\text{WS}_2$  quantum dots [1] and are assigned to the direct gap ( $\sim 3.16$  eV) of monolayered  $\text{WS}_2$  quantum dots and to defect levels, respectively. Then, the shift observed in the emission peaks is due to the additional emission contributions originated from new defect levels, which generates the main emissions at around 430 and 461 nm in the  $\text{WS}_2$  nanostructures loaded with PdO or PtO NPs, respectively. It was reported that presence of PdO or PtO NPs changes the electronic band structure of  $\text{WS}_2$  monolayers [34].

X-ray photoelectron spectroscopy was used to explore the chemical composition of the sample surface. Herein, pristine, and loaded samples

were analysed and compared with the sulfurized samples. The XPS survey spectra show the presence of W, C and O in  $\text{WO}_3$  while for  $\text{WS}_2$ , an additional signal associated with the presence of sulphur atoms is observed [Fig. S3]. The core-level regions recorded with higher energy resolution allow determining the oxidation state of the elements. The spectrum recorded in the W 4f binding energy region of  $\text{WO}_3$  samples is well reproduced by three components centred at binding energies 35.9 eV, 38.0 eV and 41.8 eV corresponding to  $W 4f_{7/2}$ ,  $W 4f_{5/2}$  and  $W 5p_{3/2}$  core energy levels, respectively (Fig. 7a, b). These binding energy values indicate the (6+) valence state, in both  $\text{WO}_3$ : PtO and  $\text{WO}_3$ : PdO samples [35].

To reproduce the W 4f peak of the  $\text{WS}_2$  samples an additional

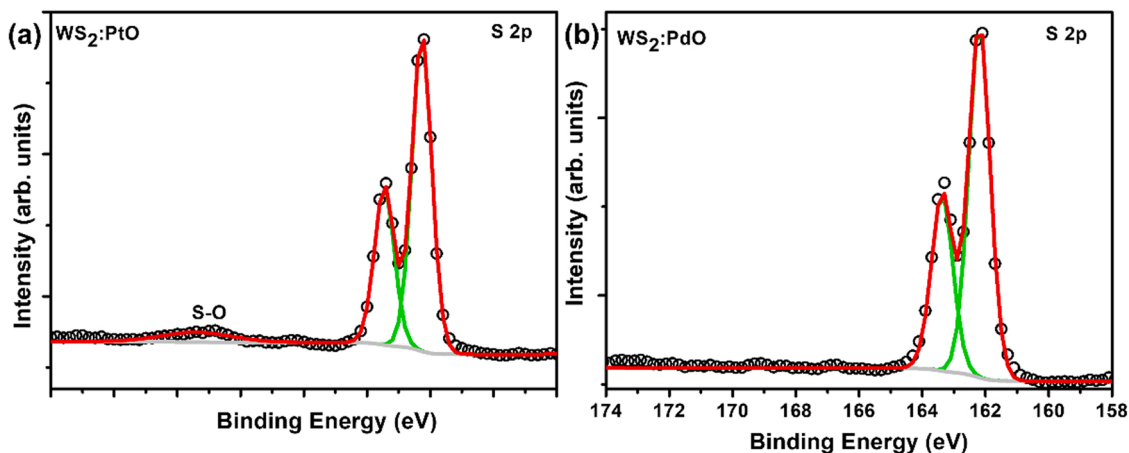


Fig. 8. XPS S 2p core level (a)  $\text{WS}_2$ : PtO (b)  $\text{WS}_2$ : PdO.

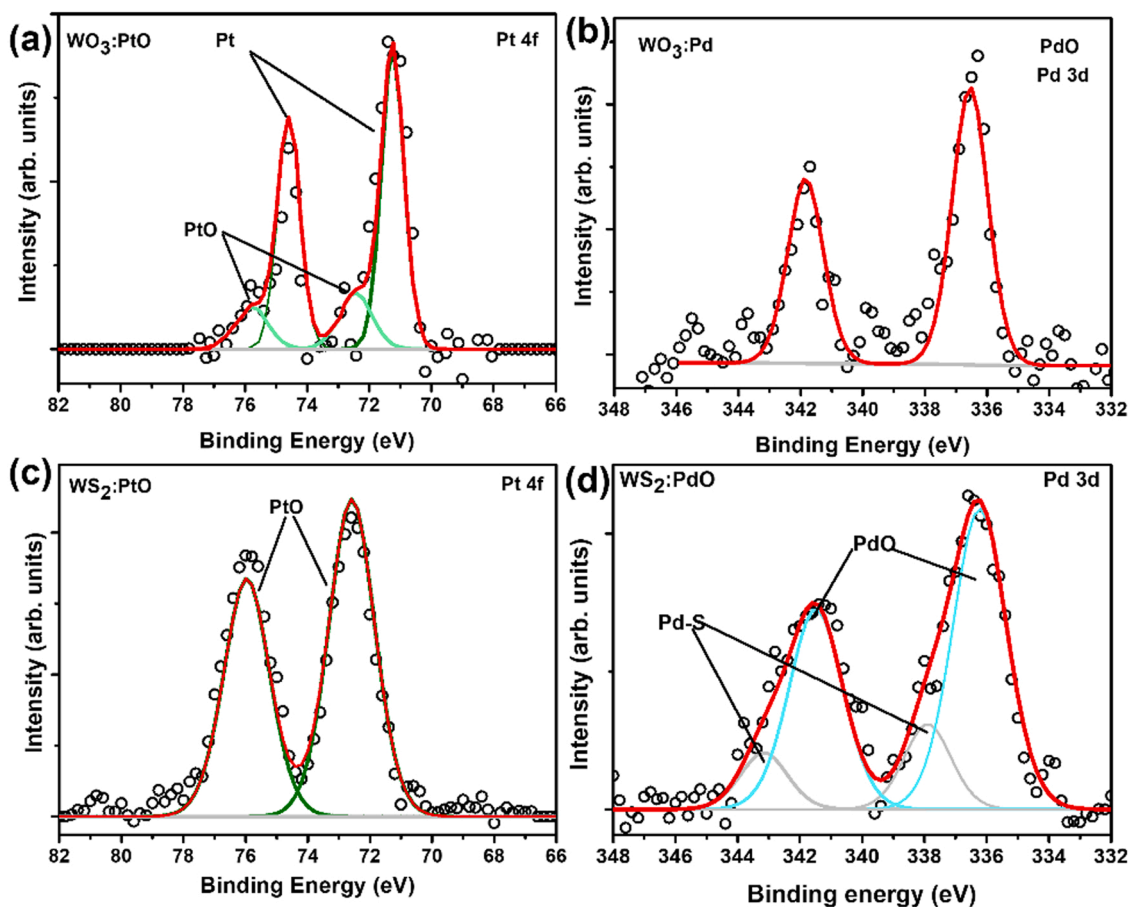


Fig. 9. XPS core level spectra: (a) PtO 4f region in  $\text{WO}_3$ : PtO (b) 3d PdO region in  $\text{WO}_3$ : PdO (c) PtO 4f region in  $\text{WS}_2$ : PtO and (d) 3d PdO region in  $\text{WS}_2$ : PdO.

doublet with components centred at 32.4 eV ( $W4f_{7/2}$ ) and 34.6 eV ( $W4f_{5/2}$ ) was used, this high-intensity doublet demonstrates the presence of tungsten atoms in the (4 +) valence state in  $\text{WS}_2$  (Fig. 7c,d) [36]. The low-intensity doublet indicates the presence of  $\text{WO}_3$  in a very small quantity which is sometimes present as an impurity, also observed in our [33] previous research work. The S 2p spectra show the presence of S-O bonds (S2p at 168.8 eV) [36] in the  $\text{WS}_2$ :PtO, though S-W ( $S2p_{1/2}$  and  $S2p_{3/2}$ , respectively at 163.3 eV and 162.) [33] is most of the bonding confirming the formation of  $\text{WS}_2$  in both samples (Fig. 8a, b). Fig. 9 shows the Pd and Pt XPS core level spectra of the  $\text{WO}_3$  samples. The Pd 3d doublet peak with components centred at 336.5 eV ( $3d_{5/2}$ ) and

341.8 eV ( $3d_{3/2}$ ) suggests the formation of PdO [37]. The Pt 4f peak is reproduced by two doublets, one with components at 71.2 eV ( $4f_{7/2}$ ) and 74.5 eV ( $4f_{5/2}$ ) indicating the presence of metallic Pt and the other with components at 72.5 eV ( $4f_{7/2}$ ) and 75.8 eV ( $4f_{5/2}$ ) associated with the formation of PtO and PtS [37]. Indeed, these two materials have narrow binding energies [37,38] and by considering the synthesis method and the FWHM of the Pt 4F we suggest that both materials coexist. The Pd and Pt core level XPS spectra recorded on  $\text{WS}_2$  samples are shown in Fig. 9c and d. The Pd 3d spectrum is reproduced by two doublets related to the presence of PdO (336.5 eV ( $3d_{5/2}$ ) and 341.8 eV ( $3d_{3/2}$ )) and the formation of Pd-S bonding (337.0 eV ( $3d_{5/2}$ ) and

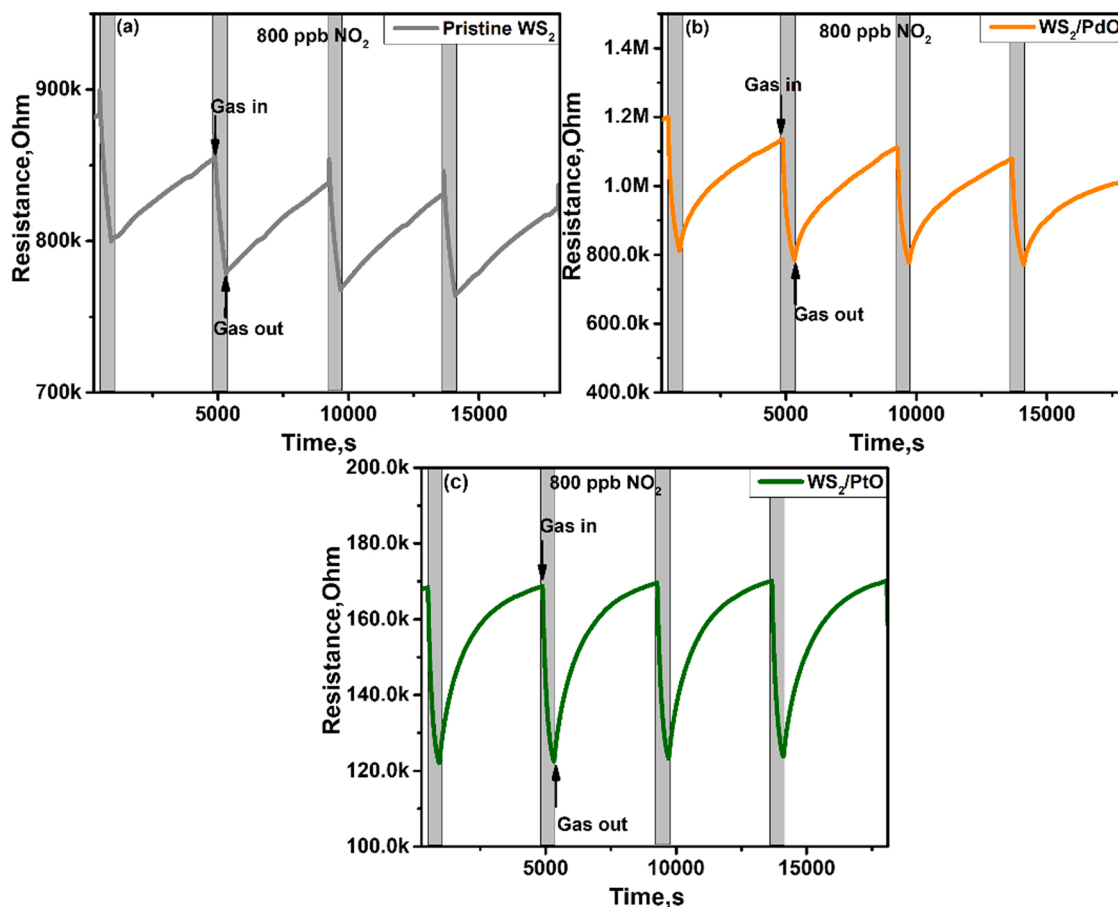


Fig. 10. Pristine WS<sub>2</sub> (grey), WS<sub>2</sub>/PdO (orange), WS<sub>2</sub>/PtO (olive), 4 replicate response and recovery cycles towards 800 ppb of NO<sub>2</sub> at room temperature.

343.6 eV (*3d<sub>3/2</sub>*) [39].

Thus, Raman, PL, XRD, XPS, TEM and FESEM results show good accordance between them and confirm the formation of WS<sub>2</sub>, WS<sub>2</sub>/PdO and WS<sub>2</sub>/PtO with the presence of some WO<sub>3</sub> impurities produced by the uncompleted sulfurization of the initial WO<sub>3</sub> nanomaterial as well as the presence of a small quantity of oxygen within the quartz tube where the experiment is conducted.

### 3.2. Gas sensing results

#### NO<sub>2</sub> Gas

The gas sensing characteristics of loaded and pristine sensing films (WS<sub>2</sub>, WS<sub>2</sub>/PtO, WS<sub>2</sub>/PdO) to both oxidising (NO<sub>2</sub>), as well as reducing (NH<sub>3</sub>, H<sub>2</sub>, CO, H<sub>2</sub>S) gases, has been analysed using a homemade gas-sensing detection system as described above (Fig. 1). The performances of the as-fabricated sensors were determined at room temperature utilising dry air balance. To calculate the sensor response towards oxidising gas, we have used equation-1 whereas in the case of reducing gases the sensor response is calculated using equation-2, given as:

$$R = \frac{(R_{air} - R_{gas})}{R_{air}} * 100 \quad (1)$$

$$R = \frac{(R_{gas} - R_{air})}{R_{air}} * 100 \quad (2)$$

Accordingly, as shown in Fig. 10 we exposed both loaded and pristine WS<sub>2</sub> films towards 800 ppb of NO<sub>2</sub>. It is worth noting that this is the highest gas concentration tested, and it is still well below the NO<sub>2</sub> exposure limit recommended by the American Conference of Government Industrial Hygienists [6]. For the three different materials operated at room temperature, Fig. 10a-c displays the dynamic film

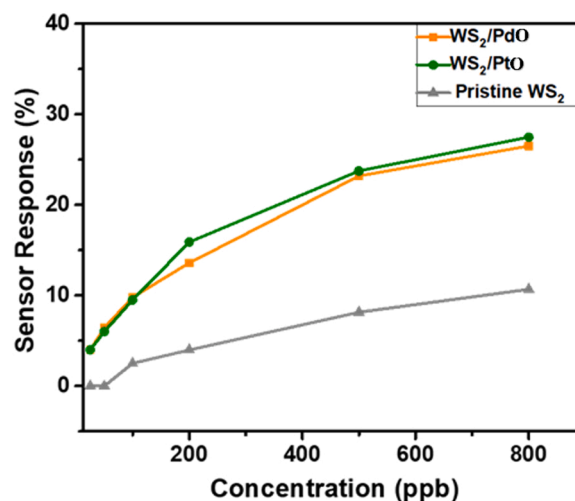


Fig. 11. Gas sensing response of pristine WS<sub>2</sub> (grey) WS<sub>2</sub>/Pd (orange), WS<sub>2</sub>/Pt (olive) as a function of NO<sub>2</sub> gas concentration at room temperature.

resistance change towards 800 ppb NO<sub>2</sub> gas. The figure clearly shows that when exposed to an oxidising type of gas, such as NO<sub>2</sub>, sensors exhibit a decrease in their electrical resistance, thereby indicating a p-type semiconducting behaviour for all of them. This is in good accordance with the findings of our previous study, in which pristine WS<sub>2</sub> sensors exhibited similar p-type behaviour [33]. While the response of the pure WS<sub>2</sub> sensor is 10.68%, one of the loaded sensors, WS<sub>2</sub>/PdO and WS<sub>2</sub>/PtO, is much greater, reaching 26.5% and 27.5%, respectively.



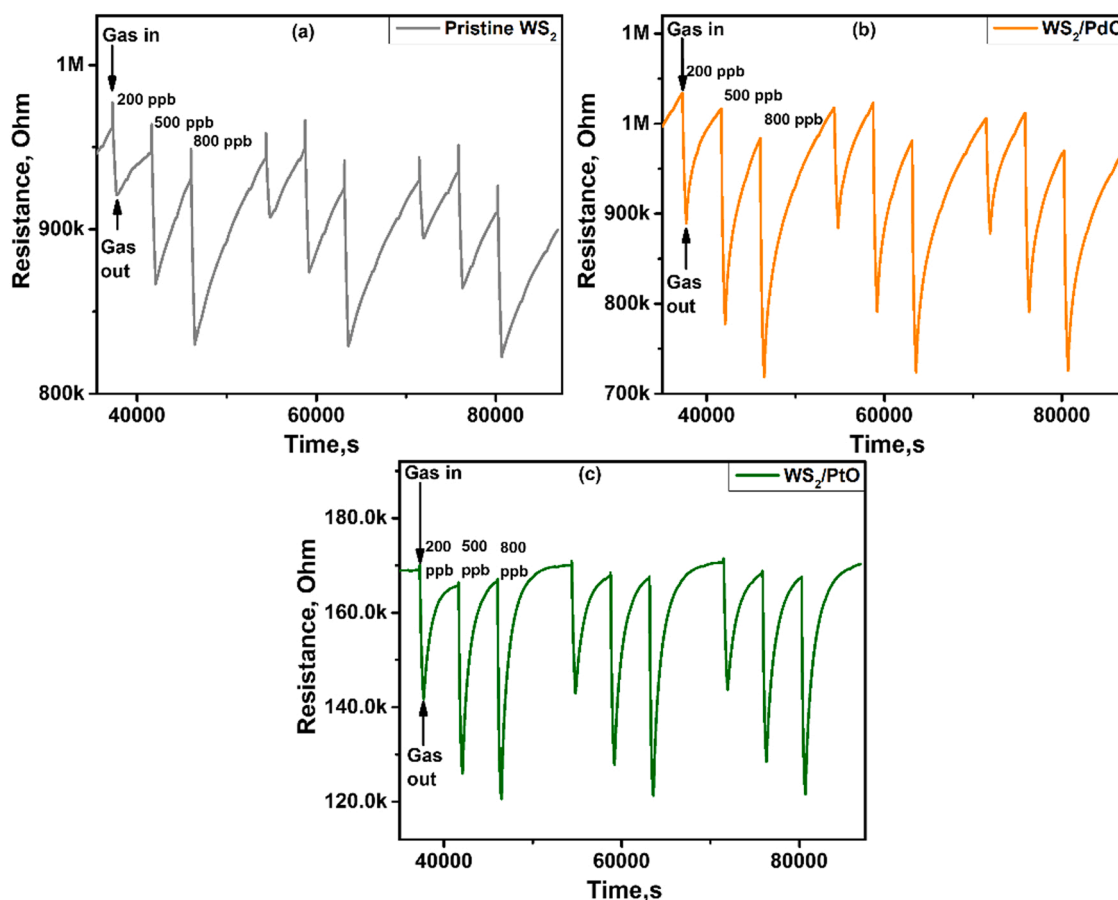


Fig. 12. Electrical resistance change of (a) pristine WS<sub>2</sub> (grey), (b) WS<sub>2</sub>/PdO (orange) and (c) WS<sub>2</sub>/PtO (olive) towards pulses of increasing concentrations of NO<sub>2</sub> gas (from 200 to 800 ppb), operated at room temperature.

At this concentration, all three sensors showed consistent and replicable responses where the maximum response was recorded from the loaded ones. Furthermore, during the recovery cycle, when the target gas is removed and the sensors are only exposed to dry air, they return completely to their baseline resistance, which is shown in Fig. 10. We also exposed pristine and loaded WS<sub>2</sub> sensors to various NO<sub>2</sub> gas concentrations. Fig. 11 displays the sensor response as a function of NO<sub>2</sub> concentrations. The experimental results for pristine WS<sub>2</sub> are equivalent to those obtained in our previous study for WS<sub>2</sub> NT sensors [33]. In contrast, both loaded sensors (PdO and PtO) perform similarly and display an enhanced sensing response towards NO<sub>2</sub> gas detection when compared to pristine WS<sub>2</sub>.

Furthermore, Fig. 12a-c shows three replicate measurements cycles to increasing concentration pulses of NO<sub>2</sub> ranging from 200 to 800 ppb in a background of dry air. During each cycle, sensors were exposed to three different concentrations of NO<sub>2</sub> while operated at room temperature. The results show an increase in sensing response with each increment in analyte concentration. The sensing response for pristine WS<sub>2</sub> was calculated to be 4%, 8.1%, 10.7% towards 200, 500 and 800 ppb of nitrogen dioxide, respectively. Again, responses for WS<sub>2</sub>/PdO and WS<sub>2</sub>/PtO were very similar. These were calculated to be 15.9%, 23.8% and 27.5% for WS<sub>2</sub>/PtO and 13.6%, 23% and 27% for WS<sub>2</sub>/PdO towards 200, 500 and 800 ppb of nitrogen dioxide, respectively. It can be observed from Fig. 12 that the response for WS<sub>2</sub>/PtO is significantly more stable because this sensor completely regains its initial baseline resistance after each cycle of measurement. These results encouraged us to explore the NO<sub>2</sub> gas sensing characteristics towards NO<sub>2</sub> at the much lower concentrations of 50 and 25 ppb. The responses of the three sensors to very low NO<sub>2</sub> gas concentrations (25 and 50 ppb) at room temperature are shown in Fig. 13a-c and Fig. S4. To test repeatability,

four consecutive replicate measurements and recovery sequences were performed. The results demonstrate that both PdO and PtO loaded WS<sub>2</sub> sensors have an adequate response to NO<sub>2</sub> for a concentration as low as 25 ppb, whereas the pristine sensor stays unresponsive until the gas concentration is increased to 100 ppb. At such a low concentration, the sensing response of the loaded sensors was reproducible and was reported to be practically equal with a value of 4%. However, at such low response signals and because the desorption of the gas molecules at room temperature is difficult, considerable drift in the response was detected for the loaded sensors.

Hence, it is observed that loading improves (i.e. lowers) the detection limit (LoD) of pristine WS<sub>2</sub> sensors. While the NO<sub>2</sub> LoD for pristine WS<sub>2</sub> sensors is 100 ppb, the LoD is lower than 25 ppb for the loaded sensors. To the best of our knowledge, such a low detection limit under 25 ppb of NO<sub>2</sub> had never been reported before using either loaded or pristine WS<sub>2</sub> nanomaterials operated at room temperature.

#### Selectivity test

In addition to NO<sub>2</sub> gas sensing studies, the performance of pristine WS<sub>2</sub>, WS<sub>2</sub>/PtO and WS<sub>2</sub>/PdO sensors were investigated for reducing gases such as, H<sub>2</sub>, CO, NH<sub>3</sub>, H<sub>2</sub>S to determine the potential selectivity of each sensor towards NO<sub>2</sub> gas detection. Fig. S5 illustrates typical response and recovery cycles for each gas.

The histogram in Fig. 14 summarises the results obtained from the selectivity measurements for each material. MOX loading clearly enhances the response towards NO<sub>2</sub> and diminishes the cross-sensitivity towards ammonia and hydrogen sulphide observed in pristine WS<sub>2</sub>. WS<sub>2</sub>/PtO shows some cross-sensitivity towards H<sub>2</sub> and CO. However, considering that possible interfering species were measured at significantly higher concentrations than that of NO<sub>2</sub>, it can be derived that the loading has improved selectivity towards nitrogen dioxide.

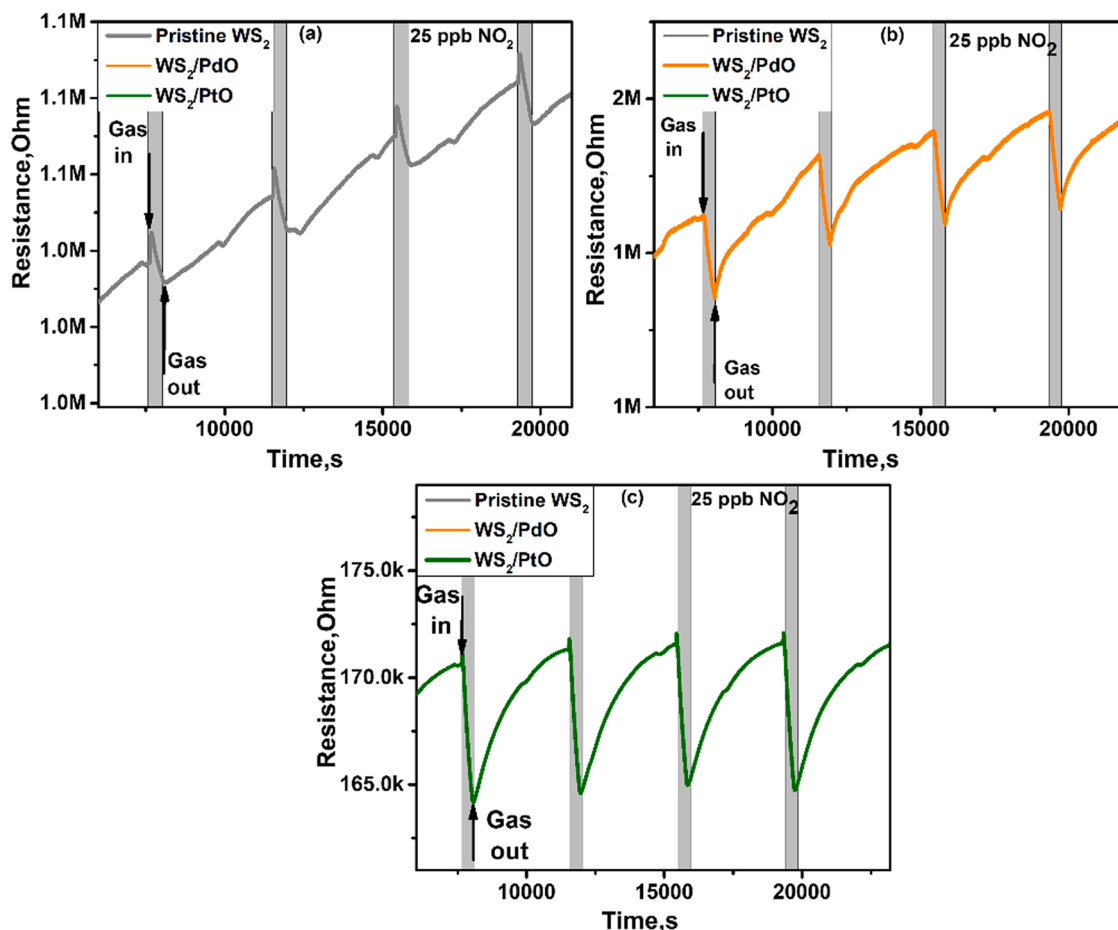


Fig. 13. Electrical resistance change of (a) pristine WS<sub>2</sub> (grey), (b) WS<sub>2</sub>/PdO (orange) and (c) WS<sub>2</sub>/PtO (olive) towards NO<sub>2</sub> at 25 ppb, operated at room temperature.

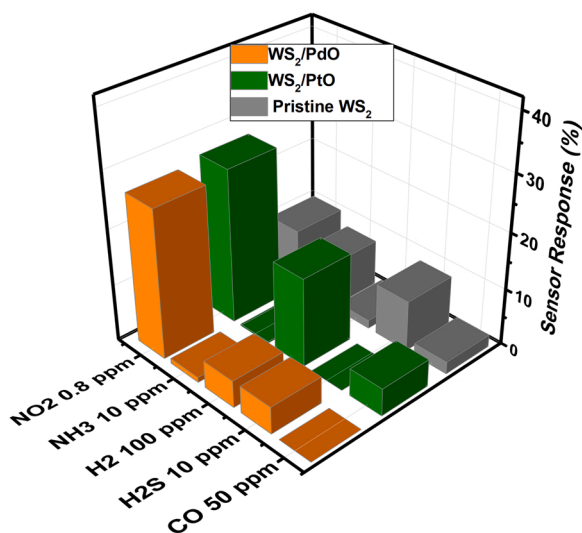


Fig. 14. Response histogram of pristine WS<sub>2</sub>, WS<sub>2</sub>/PdO and WS<sub>2</sub>/PtO sensors towards NO<sub>2</sub> (0.8 ppm), NH<sub>3</sub> (10 ppm), H<sub>2</sub> (100 ppm), H<sub>2</sub>S (10 ppm) and CO (50 ppm) gas, at room temperature.

#### Humidity.

The influence of humidity on the sensor response towards NO<sub>2</sub> has also been studied. The sensors were tested towards 0.8 ppm NO<sub>2</sub> at room temperature in a 50% humidified background (@ 21°C), and the results

are presented in Fig. 15. According to the findings, all three sensors have different responses to humidity. For example, the pristine WS<sub>2</sub> sensor, as well as the PdO/WS<sub>2</sub> sensor, showed enhanced gas sensing response, with the PdO/WS<sub>2</sub> sensor response increasing from 26.5% to 54% and the pristine WS<sub>2</sub> sensor response increasing from 10.68% to 53%. However, the PtO/WS<sub>2</sub> sensor, on the other hand, exhibited a completely different behaviour, with sensor response dropping from 27.5% to only 3%. Based on the literature, it is suggested that when PtO/WS<sub>2</sub> sensor is exposed to humidity, the OH<sup>-</sup> occupy most of the active sites that were previously available for the interaction with NO<sub>2</sub> gas molecules. As a result, the access of NO<sub>2</sub> gas molecules to the surface-active sites is reduced [40]. Thereby resulting in negligible sensing response (3%) under a humid atmosphere. Regarding pristine as well as PdO/WS<sub>2</sub> sensor, the effect of humidity is quite different, as both sensors showed enhanced gas sensing responses towards NO<sub>2</sub>. This behaviour has been reported earlier for WS<sub>2</sub> nanoflakes based gas sensor towards NH<sub>3</sub> detection [42]. They suggested that the enhancement observed in the sensor response is due to the sulphides-ions assisted hydroxylation of the co-adsorbed water molecules and due to the oxidation of the solvated ammonia with adsorbed oxygen ions on the surface of WS<sub>2</sub> nanoflakes. Another study reports WS<sub>2</sub>/graphene aerogel-based sensor, where the sensor response towards NO<sub>2</sub> increases when humidity increases [41]. They interpret this behaviour by Grotthius transport mechanism where the resistance change is related to the movement of protons H<sup>+</sup> or H<sub>3</sub>O<sup>+</sup> within the physisorbed water molecules. Since all the measurements were done at room temperature, the migration of protons becomes much easier, which results in a further decrease in film resistance, thereby increasing sensor response towards NO<sub>2</sub> detection.

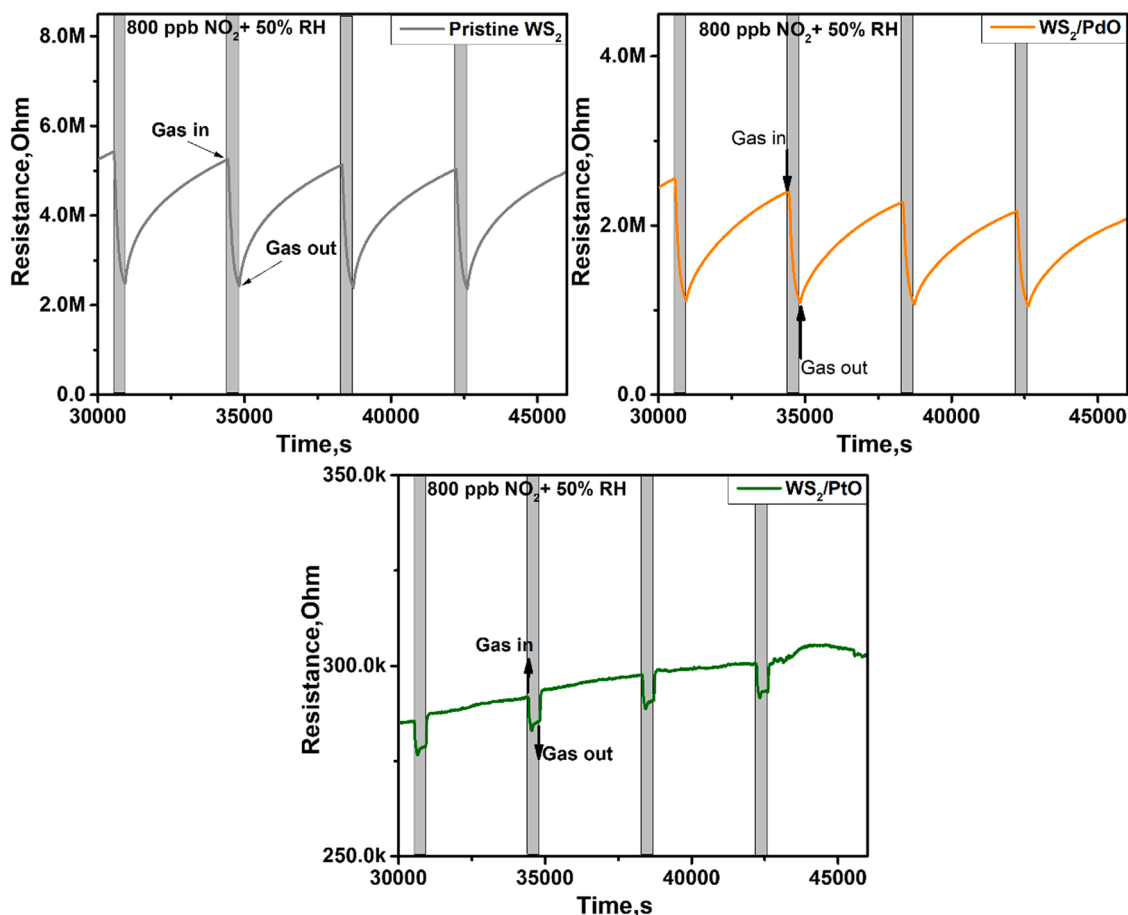


Fig. 15. Relative humidity (50%) cross-sensitivity of pristine WS<sub>2</sub>, WS<sub>2</sub>/PdO and WS<sub>2</sub>/PtO sensors towards 0.8 ppm NO<sub>2</sub>, at room temperature.

The behaviour of TMD gas sensors under humid conditions is not deeply studied and needs to be further explored.

After the humidity was removed from the background, all sensors regained their original sensing response after applying mild heating (100 °C) for 4–5 h and the corresponding results are presented in Fig. S6. These results also indicate that PdO/WS<sub>2</sub> shows the best NO<sub>2</sub> sensing characteristics among the different materials tested. This difference observed in the gas sensing properties between the loaded sensors can be attributed to the metal used as well as the size of the nanoparticles. Additionally, a stability study was performed by exposing the sensors towards 0.8 ppm NO<sub>2</sub> at room temperature for 6 weeks (Fig. S6) and all three materials showed good stability.

#### 4. Gas sensing mechanisms

##### 4.1. Detection of nitrogen dioxide

NO<sub>2</sub> molecules are electron acceptors and H<sub>2</sub>S, H<sub>2</sub>, CO or NH<sub>3</sub> are electron donors. The resistance of the different WS<sub>2</sub> devices decreases in the presence of NO<sub>2</sub> and increases in the presence of the above-mentioned electron donor species. This is indicative that our pure or loaded tungsten disulphide samples behave as p-type semiconducting materials. The n-type or p-type nature of WS<sub>2</sub> depends on its morphology, nanostructure alignment on the substrate or even on the presence of few carbon atoms substituting sulfur atoms [29,30]. The p-type behaviour of WS<sub>2</sub> achieved via the sulfurization of WO<sub>3</sub> has been reported previously [33,45]. The nitrogen dioxide sensing mechanism in WS<sub>2</sub> involves the adsorption of NO<sub>2</sub> molecules both on the edges of flakes and on their surface (or basal plane). Upon adsorption, an electronic charge is injected from WS<sub>2</sub> towards the gas molecule, which

generates a hole accumulation zone that results in a decrease in the resistance of the film. According to previously reported computational chemistry studies in MoS<sub>2</sub>, the edges are far more important than the basal plane for the adsorption of NO<sub>2</sub>, because the adsorption energy of nitrogen dioxide at S edges is about 4 times higher than at the basal plane and so is the associated electronic charge transfer [46]. The computed adsorption energies suggest that the interaction between WS<sub>2</sub> and NO<sub>2</sub> involves the physisorption of nitrogen dioxide. This is supported by the experimental results showing that sensor baseline resistance can be regained when flowing the sensor surface with clean air when sensors are operated at room temperature.

PL analysis conducted on pure WO<sub>3</sub> and PtO or PdO loaded WO<sub>3</sub> indicates that PtO or PdO loaded tungsten oxide have an increased number of defects in comparison to pure tungsten oxide. Since WS<sub>2</sub> is achieved via the sulfurization of tungsten oxide samples, these additional defects translate into an increased number of S edges in PtO or PdO loaded WS<sub>2</sub>. Indeed, the PL studies have shown that PtO and PdO loaded WS<sub>2</sub> samples are characterized by a redshift of the PL maximum and by a higher FWHM in comparison to the one for pure WS<sub>2</sub> samples, which can be associated with a higher number of defects being present in loaded samples. This explains why PtO and PdO loaded WS<sub>2</sub> show significantly higher responses to NO<sub>2</sub> than pure WS<sub>2</sub>.

Some authors have reported that platinum and palladium oxide nanoparticles supported on a semiconducting nanomaterial play a role in the sensitization of this nanomaterial to NO<sub>2</sub>. These authors described both electronic and chemical sensitization effects for explaining the increased responses towards nitrogen dioxide observed [47,48]. PtO and PdO were found on the surface of loaded WS<sub>2</sub> samples by XPS (also detected by XRD). Therefore, the presence of such oxides could also contribute to the enhanced NO<sub>2</sub> response shown by PtO or PdO loaded



WS<sub>2</sub>.

#### 4.2. Response to hydrogen

Besides the significant improvement in the response towards nitrogen oxide observed for PtO or PdO loaded WS<sub>2</sub> samples, a small increase in response towards hydrogen was observed too. Platinum and palladium oxides are p-type materials well known for acting as chemical and/or electronic sensitizers towards hydrogen when dispersed in n-type metal oxides [30] and this may be the reason why PtO or PdO loaded WS<sub>2</sub> samples show an increased response towards hydrogen in comparison to the one of pure WS<sub>2</sub>. However, as already stated, this response increase is rather moderate. The sulfurization of PtO and PdO oxides results in PtS and PdS, which hinders the above-described hydrogen sensitization effect. While the presence of PdS was confirmed both by XPS and XRD, PtS could be confirmed by XRD only. These results indicate that PtS is found in lower quantities than PdS, which explains why PtO loaded WS<sub>2</sub> is slightly more sensitive to hydrogen than PdO loaded WS<sub>2</sub>.

#### 5. Conclusion

We have been able to develop a unique method to fabricate loaded WS<sub>2</sub> directly on commercial sensor substrate via a combination of AACVD and CVD techniques. This co-deposition approach demonstrates an effective route to bring functionality in metal sulphides. Metal-oxide loaded sensors are composed of a hybrid structure of nanoneedles and nanosheets of WS<sub>2</sub> with high quality and crystallinity, as determined by Raman, XRD, and FESEM characterization techniques, and either a combination of PtO and PtS or PdO and PdS NPs are present between its surface, as determined by TEM, XRD and XPS spectroscopy. Moreover, we have investigated the gas sensing performance of both loaded sensors and unloaded sensor. The electrical characteristics of pristine WS<sub>2</sub> were tuned through loading with metal-oxide ions. It is fascinating to know that all the gas sensing measurements were carried out at room temperature and the WS<sub>2</sub>-based gas sensors exhibited stable, reproducible, and ultrasensitive responses towards NO<sub>2</sub> at ppb concentration levels. The sensing results revealed that loading of WS<sub>2</sub> nanosheets with either PtO or PdO ions significantly increases their gas response towards NO<sub>2</sub> (i.e., double the response as compared to pristine WS<sub>2</sub> sensor from 10% to 26.5%, thereby lowering the detection limit of the sensor (lower than 25 ppb after loading, which is far lower than that of pristine WS<sub>2</sub> gas sensor). To our knowledge, no previous research has used a loaded or pristine WS<sub>2</sub> nanomaterial to obtain such a low detection limit of 25 ppb of NO<sub>2</sub> at room temperature. Even though the sensor displayed considerable humidity cross-sensitivity at room temperature, once the moisture was removed with mild heating, it regained its original sensing response, demonstrating its outstanding NO<sub>2</sub> gas detection properties. Moreover, when compared to the WS<sub>2</sub>/PtO sensor, the WS<sub>2</sub>/PdO sensor is extremely selective for NO<sub>2</sub>, exhibiting little or no response to other gases. In the end, the synthesis methodology adopted during this study is promising to incorporate metal-oxide ions on transition metal dichalcogenides. Henceforth, we believe, the results obtained in this study at room temperature are intriguing and encouraging in terms of developing a sensitive, cost-effective, and energy-efficient NO<sub>2</sub> gas sensor.

#### Credit authorship contribution statement

**Aanchal Alagh:** Investigation, Formal analysis, Data curation, Writing – original draft. **Fatima Ezahra Annanouch:** Conceptualization, Supervision, Writing – review & editing. **Khaled Al Youssef:** Investigation and Data curation. **Carla Bittencourt:** Investigation and Data curation. **Frank Güell:** Investigation and Data curation. **Paulina R. Martínez-Alanis:** Investigation and Data curation. **Marc Reguant:** Investigation and Data curation. **Eduard Llobet:** Conceptualization, Supervision, Writing – review & editing, Funding acquisition.

#### Declaration of Competing Interest

The authors declare that they have no known competing financial interests or personal relationships that could have appeared to influence the work reported in this paper.

#### Acknowledgements

Funded in part by the Marie Skłodowska-Curie Actions (MSCA) Research and Innovation Staff Exchange (RISE) H2020-MSCA-RISE-2018- 823895 ‘SENSoft’, by MICINN and FEDER grant no. RTI2018-101580-I00 and AGAUR grant no. 2017 SGR 418. A.A. is supported by a COFUND project the European Union’s Horizon 2020 research and innovation program under the Marie Skłodowska-Curie grant agreement No. 713679 and the Universitat Rovira i Virgili (URV). C.B. is a Research Associate of the National Funds for Scientific Research (FRS-FNRS, Belgium; E.L. is supported by the Catalan Institute for advanced studies (ICREA) via the 2018 Edition of the ICREA Academia Award.

#### Appendix A. Supporting information

Supplementary data associated with this article can be found in the online version at doi:10.1016/j.snb.2022.131905.

#### References

- [1] D.Galán Madruga, Importance of air quality networks in controlling exposure to air pollution, *Environ. Emiss.* (2021) 1–15, <https://doi.org/10.5772/intechopen.92335>.
- [2] S.J. Jung, J.S. Mehta, L. Tong, Effects of environment pollution on the ocular surface, *Ocul. Surf.* 16 (2) (2018) 198–205, <https://doi.org/10.1016/j.jtos.2018.03.001>.
- [3] J.H. Kim, A. Mirzaei, H.W. Kim, S.S. Kim, Flexible and low power CO gas sensor with Au-functionalized 2D WS<sub>2</sub> nanoflakes (December), *Sens. Actuators, B Chem.* 313 (no) (2019), 128040, <https://doi.org/10.1016/j.snb.2020.128040>.
- [4] New Jersey Department of Health and Senior Services, “Hazardous Substance Fact Sheet, Nitrogen Dioxide,” 1989, [Online]. Available: <https://nj.gov/health/eoh/rtkweb/documents/fs/1376.pdf>.
- [5] J.P. Frawley, Emergency exposure limits American industrial hygiene association, toxicology committee, *Am. Ind. Hyg. Assoc. J.* 25 (6) (1964) 578–586, <https://doi.org/10.1080/00028896409342646>.
- [6] A. Momen, et al., Robust room-temperature NO<sub>2</sub> sensors from exfoliated 2D few-layered CVD-grown bulk tungsten diselenide (2H-WSe<sub>2</sub>), *ACS Appl. Mater. Interfaces* 13 (3) (2021) 4316–4329, <https://doi.org/10.1021/acsami.0c17924>.
- [7] H. Luo, et al., Design of p–p heterojunctions based on CuO decorated WS<sub>2</sub> nanosheets for sensitive NH<sub>3</sub> gas sensing at room temperature, *Nanotechnology* 32 (44) (2021), 445502, <https://doi.org/10.1088/1361-6528/ac1800>.
- [8] J. Sun, et al., Synthesis methods of two-dimensional MoS<sub>2</sub>: a brief review, *Crystals* 7 (7) (2017) 1–11, <https://doi.org/10.3390/cryst7070198>.
- [9] S. Vallejos, et al., Single-step deposition of Au- and Pt-nanoparticle-functionalized tungsten oxide nanoneedles synthesized via aerosol-assisted CVD, and used for fabrication of selective gas microsensor arrays, *Adv. Funct. Mater.* 23 (10) (2013) 1313–1322, <https://doi.org/10.1002/adfm.201201871>.
- [10] D. Andrzejewski, et al., Flexible large-area light-emitting devices based on WS<sub>2</sub> monolayers, *Adv. Opt. Mater.* 8 (20) (2020) 5–9, <https://doi.org/10.1002/adom.202000694>.
- [11] R. Levi, O. Bitton, G. Leitner, R. Tenne, E. Joselevich, Field-effect transistors based on WS<sub>2</sub> nanotubes with high current-carrying capacity, *Nano Lett.* 13 (8) (2013) 3736–3741, <https://doi.org/10.1021/nl401675k>.
- [12] M. Ikram, et al., Fabrication and characterization of a high-surface area MoS<sub>2</sub>@WS<sub>2</sub> heterojunction for the ultra-sensitive NO<sub>2</sub> detection at room temperature, *J. Mater. Chem. A* 7 (24) (2019) 14602–14612, <https://doi.org/10.1039/c9ta03452h>.
- [13] J.H. Kim, A. Mirzaei, H.W. Kim, S.S. Kim, Realization of Au-decorated WS<sub>2</sub> nanosheets as low power-consumption and selective gas sensors, *Sensors Actuators, B Chem.* 296 (June) (2019), 126659, <https://doi.org/10.1016/j.snb.2019.126659>.
- [14] Y. Ren, et al., Noble metal nanoparticles decorated metal oxide semiconducting nanowire arrays interwoven into 3D mesoporous superstructures for low-temperature gas sensing, *ACS Cent. Sci.* 7 (11) (2021) 1885–1897, <https://doi.org/10.1021/acscentsci.1c00912>.
- [15] S. Park, P.M. Bulemo, W.T. Koo, J. Ko, I.D. Kim, “Chemiresistive acetylene sensor fabricated from Ga-doped ZnO nanofibers functionalized with Pt catalysts (May), in: *Sensors Actuators, B Chem.*, vol. 343, 2021, 130137, <https://doi.org/10.1016/j.snb.2021.130137> (May).
- [16] J. Guo, S. Wang, Z. Lin, L. Liu, Y. Hui, Ultrasensitive acetone sensor based on holey zinc oxide nanosheets doped by gold nanoparticles (July), *Mater. Lett.* 302 (no) (2021), 130443, <https://doi.org/10.1016/j.matlet.2021.130443>.

- [17] A. Hermawan, N.L.W. Septiani, A. Taufik, B. Yulianto, Suyatman, S. Yin, *Advanced Strategies to Improve Performances of Molybdenum-Based Gas Sensors*, vol. 13, Springer, Singapore, 2021.
- [18] K.Y. Ko, et al., "Improvement Gas. -Sens. Perform. Large-Area Tungsten Disulfide Nanosheets Surf. Funct.," (2016), <https://doi.org/10.1021/acsnano.6b03631>.
- [19] D. Zhang, Y. Cao, J. Wu, X. Zhang, Tungsten trioxide nanoparticles decorated tungsten disulfide nanoheterojunction for highly sensitive ethanol gas sensing application (August), *Appl. Surf. Sci.* 503 (no) (2019), 144063, <https://doi.org/10.1016/j.apsusc.2019.144063>.
- [20] A. Alagh, F.E. Annanouch, P. Umek, C. Bittencourt, J.F. Colomer, E. Llobet, An ultrasensitive room-temperature HS gas sensor based on 3D assembly of CuO decorated WS nanomaterial, *IEEE Sens. J.* 21 (19) (2021) 21212–21220, <https://doi.org/10.1109/JSEN.2021.3103925>.
- [22] M. Chen, et al., Stable few-layer MoS<sub>2</sub> rectifying diodes formed by plasma-assisted doping, *Appl. Phys. Lett.* 103 (14) (2013), <https://doi.org/10.1063/1.4824205>.
- [23] M.R. Laskar, et al., P-type doping of MoS<sub>2</sub> thin films using Nb, *Appl. Phys. Lett.* 104 (9) (2014), <https://doi.org/10.1063/1.4867197>.
- [24] V.E. Fedorov, et al., Tuning electronic properties of molybdenum disulfide by a substitution in metal sublattice," 2013 36th Int. Conv. Inf. Commun. Technol. Electron. Microelectron. MIPRO 2013 - Proc. 2 (2013) 11–14.
- [25] A. Alagh, et al., CVD growth of self-assembled 2D and 1D WS<sub>2</sub> nanomaterials for the ultrasensitive detection of NO<sub>2</sub> (April), *Sens. Actuators, B Chem.* 326 (2020), 128813, <https://doi.org/10.1016/j.snb.2020.128813>.
- [26] H. Fang, S. Chuang, T.C. Chang, K. Takei, T. Takahashi, A. Javey, High-performance single layered WSe<sub>2</sub> p-FETs with chemically doped contacts, *Nano Lett.* 12 (7) (2012) 3788–3792, <https://doi.org/10.1021/nl301702r>.
- [27] S. Tongay, et al., Broad-range modulation of light emission in two-dimensional semiconductors by molecular physisorption gating, *Nano Lett.* 13 (6) (2013) 2831–2836, <https://doi.org/10.1021/nl4011172>.
- [28] Y. Li, C. Xu, P. Hu, L. Zhen, Carrier control of MoS<sub>2</sub> nanoflakes by, *ACS Nano* 7 (9) (2013) 7795–7804.
- [29] S. Mouri, Y. Miyauchi, K. Matsuda, Tunable photoluminescence of monolayer MoS<sub>2</sub> via chemical doping, *Nano Lett.* 13 (12) (2013) 5944–5948, <https://doi.org/10.1021/nl403036h>.
- [30] F.E. Annanouch, et al., Aerosol-assisted CVD-grown PdO nanoparticle-decorated tungsten oxide nanoneedles extremely sensitive and selective to hydrogen, *ACS Appl. Mater. Interfaces* 8 (16) (2016) 10413–10421, <https://doi.org/10.1021/acsami.6b00773>.
- [31] F.E. Annanouch, et al., Aerosol-assisted CVD-grown WO<sub>3</sub> nanoneedles decorated with copper oxide nanoparticles for the selective and humidity-resilient detection of H<sub>2</sub>S, *ACS Appl. Mater. Interfaces* 7 (12) (2015) 6842–6851, <https://doi.org/10.1021/acsami.5b00411>.
- [32] W.S. Nanomaterials, et al., Use Pulse UV Or. Visible Light Act. Gas. Sens. Reducing Oxid. Species WO<sub>3</sub> (2021).
- [33] A. Alagh, et al., CVD growth of self-assembled 2D and 1D WS<sub>2</sub> nanomaterials for the ultrasensitive detection of NO<sub>2</sub> (August), *Sens. Actuators, B Chem.* vol. 326 (no) (2020), 128813, <https://doi.org/10.1016/j.snb.2020.128813>.
- [34] X. Zhao, C. Xia, X. Dai, T. Wang, P. Chen, L. Tian, Electronic and magnetic properties of X-doped (X=Ni, Pd, Pt) WS<sub>2</sub> monolayer, *J. Magn. Magn. Mater.* 414 (2016) 45–48, <https://doi.org/10.1016/j.jmmm.2016.04.050>.
- [35] C. Navío, et al., Gold clusters on WO<sub>3</sub> nanoneedles grown via AACVD: XPS and TEM studies, *Mater. Chem. Phys.* 134 (2–3) (2012) 809–813, <https://doi.org/10.1016/j.matchemphys.2012.03.073>.
- [36] K.M. McCreary, A.T. Hanbicki, G.G. Jernigan, J.C. Culbertson, B.T. Jonker, Synthesis of large-area WS<sub>2</sub> monolayers with exceptional photoluminescence, *Sci. Rep.* 6 (2015) 1–7, <https://doi.org/10.1038/srep19159>.
- [37] G.K. Reddy, T.C. Peck, C.A. Roberts, 'PdO vs. PtO'—The influence of PGM oxide promotion of Co<sub>3</sub>O<sub>4</sub> spinel on direct NO decomposition activity, *Catalysts* vol. 9 (1) (2019), <https://doi.org/10.3390/catal9010062>.
- [38] "Dembowski, Pdf." (1993), <https://doi.org/10.1116/1.1247716>.
- [39] D. Zhao, et al., Synthesis of large-scale few-layer PtS<sub>2</sub> films by chemical vapor deposition, *AIP Adv.* 9 (2) (2019), <https://doi.org/10.1063/1.5086447>.
- [40] Y. Han, et al., Interface engineered WS<sub>2</sub>/ZnS heterostructures for sensitive and reversible NO<sub>2</sub> room temperature sensing, *Sens. Actuators, B Chem.* 296 (April) (2019), 126666, <https://doi.org/10.1016/j.snb.2019.126666>.
- [41] W. Yan, M.A. Worsley, T. Pham, A. Zettl, C. Carraro, R. Maboudian, Effects of ambient humidity and temperature on the NO<sub>2</sub> sensing characteristics of WS<sub>2</sub> /graphene aerogel, *Appl. Surf. Sci.* 450 (2018) 372–379, <https://doi.org/10.1016/j.apsusc.2018.04.185>.
- [42] X. Li, X. Li, Z. Li, J. Wang, J. Zhang, WS<sub>2</sub> nanoflakes based selective ammonia sensors at room temperature," *Sensors Actuators, B Chem.* 240 (2017) 273–277, <https://doi.org/10.1016/j.snb.2016.08.163>.
- [45] G.A. Asres, et al., "Ultrasensitive H<sub>2</sub> S Gas. Sens. Based p-Type WS<sub>2</sub> Hybrid. Mater.," (2009) 1–10.
- [46] G. Deokar, et al., MoS<sub>2</sub>-carbon nanotube hybrid material growth and gas sensing, *Adv. Mater. Interfaces* 4 (24) (2017), <https://doi.org/10.1002/admi.201700801>.
- [47] S.W. Choi, J. Kim, Y.T. Byun, Highly sensitive and selective NO<sub>2</sub> detection by Pt nanoparticles-decorated single-walled carbon nanotubes and the underlying sensing mechanism, *Sens. Actuators, B Chem.* 238 (2) (2017) 1032–1042, <https://doi.org/10.1016/j.snb.2016.07.153>.
- [48] X. Chen, et al., NO<sub>2</sub> sensing properties of one-pot-synthesized ZnO nanowires with Pd functionalization, *Sens. Actuators, B Chem.* 280 (2) (2019) 151–161, <https://doi.org/10.1016/j.snb.2018.10.063>.

**Aanchal Alagh** is a MSCA– COFUND PhD fellow at the Universitat Rovira i Virgili. Her research interest are on the synthesis and application of transition metal dichalcogenide materials.

**Fatima Ezahra Annanouch** is a Juan de la Cierva Post-Doctoral Fellow at the Universitat Rovira i Virgili. She obtained her PhD degree (2015) on the fabrication and characterization of metal oxide nanowires gas sensors, from the department of electrical electronic engineering and automation, Rovira i Virgili university (Tarragona), Spain. On 2016, she started her first postdoctoral position (2 years) at IM2NP, university of Aix-Marseille, France. Her research interests are on the synthesis and application of metal oxides and transition metal dichalcogenide materials to gas sensing.

**Khaled Al Youssef** is research within the Department of Chemistry at the University of Mons-Hainaut, Belgium. He is working on low kinetic energy irradiation of thin films prepared by various methods (CVD - Wet Chemistry procedure - mechanical exfoliation.).

**Carla Bittencourt** is Research Professor within the Department of Chemistry at the University of Mons-Hainaut, Belgium. One of her research interest is in the development of carbon based, hybrid nanomaterials for sensing gases at low operating temperatures.

**Frank Güell** received in 2005 the Ph.D. degree in Physics from Universitat de Barcelona (UB), and currently is Associate Professor at the Electronics Department of UB. During his Ph.D. and afterwards he joined several times the Max-Born-Institute for Nonlinear Optics and Ultrafast Spectroscopy in Berlin, Germany. His general area of research is in the growth and study of semiconductor nanomaterials such as ZnO nanowires. His research interests also include laser physics, optical sensors and solar cells based on nanostructures.

**Paulina R. Martínez-Alanis** obtained her Ph.D. in Science working on the field of bio-inorganic chemistry from Universidad Nacional Autónoma de México in 2012. Currently she is working on the vapor–liquid–solid growth of ZnO nanostructures at Universitat de Barcelona. She is also interested in the conversion of CO<sub>2</sub>, H<sub>2</sub>, O<sub>2</sub>, N<sub>2</sub> in to feedstock products

**Marc Reguant** is a master student at the Electronics Department of Universitat de Barcelona.

**Eduard Llobet** Eduard Llobet is a full professor at the Department of Electronic Engineering of the Universitat Rovira i Virgili in Tarragona (Spain). He was awarded a Ph.D. in 1997 from the Technical University of Catalonia (Barcelona) and then joined the Gas Sensor Lab (UWarwick, UK) for a one-year postdoc. From 2010 to 2014 he was Director of the Research Centre on Engineering of Materials and micro/nano Systems. He is currently addressing the fabrication of sensor arrays employing low-dimensional metal oxides and carbon nanomaterials. Cost-effective and industrially scalable methods are considered for bottom-up integration in MEMS or flexible platforms. The applications sought are (i) sensitive and selective gas microsenors for environmental monitoring, medicine or safety and (ii) heterogeneous catalysis. He got the ICREA Academia Award in the 2018 Edition.